2-D and 3-D Reconstruction Algorithms in the Fourier Domain for Plane-Wave Imaging in Nondestructive Testing

Lucas Merabet, Sébastien Robert, and Claire Prada

***Abstract*— Time-domain plane-wave imaging (PWI) has recently emerged in medical imaging and is now taking to nondestructive testing (NDT) due to its ability to provide images of good resolution and contrast with only a few steered plane waves. Insonifying a medium with plane waves is a particularly interesting approach in 3-D imaging with matrix arrays because it allows to tremendously reduce the volume of data to be stored and processed as well as the acquisition time. However, even if the data volume is reduced with plane wave emissions, the image reconstruction in the time domain with a delay-and-sum algorithm is not sufficient to achieve low computation times in 3-D due to the number of voxels. Other reconstruction algorithms take place in the wavenumber–frequency (*f-k*) domain and have been shown to accelerate computation times in seismic imaging and in synthetic aperture radar. In this paper, we start from time-domain PWI in 2-D and compare it to two algorithms in the *f-k* domain, coming from the Stolt migration in seismic imaging and the Lu theory of limited diffraction beams in medical imaging. We then extend them to immersion testing configurations where a linear array is facing a plane water–steel interface. Finally, the reconstruction algorithms are generalized to 3-D imaging with matrix arrays. A comparison dwelling on image quality and algorithmic complexities is provided, as well as a theoretical analysis of the image amplitudes and the limits of each method. We show that the reconstruction schemes in the *f-k* domain improve the lateral resolution and offer a theoretical and numerical computation gain of up to 36 in 3-D imaging in a realistic NDT configuration.**

***Index Terms*— 2-D and 3-D imaging, nondestructive testing (NDT), transducer arrays, ultrasounds, wavenumber–frequency (*f-k*) migration.**

I. Introduction

TWO-DIMENSIONAL real-time imaging with ultrasonic arrays has arisen about 20 years ago in nondestructive testing (NDT) and is more and more commonly utilized for on-site inspections. If real-time imaging has long been confined to focused B-scan and S-scan, recent more advanced methods have been implemented in NDT systems [1]. The most common today is the total focusing method (TFM), where the elements are excited one by one to record the inter-element impulse response matrix of the array [2], [3]. The signals contained in this matrix are then post-processed in the time domain to focus both in transmit and receive modes everywhere in the region of interest [4], [5]. Compared to conventional imaging techniques based on focused emissions, the TFM improves both the image quality and spatial resolution. More recently, the plane-wave imaging (PWI) method developed for ultrafast medical imaging [6] has been generalized to deal with realistic NDT applications such as multimodal imaging of crack-like defects or imaging under water/steel interfaces [7], [8]. One of the advantages of plane wave emissions is that only a few steered angles are sufficient to obtain an image of good quality, so that frame rates can be increased compared to the TFM. Today, 2-D imaging systems are fast enough for most of the real-time NDT applications where the transducer arrays are composed of up to 128 elements.

Whereas real-time 3-D imaging is spreading in medical imaging [9]–[11], it is almost nonexistent in NDT. This is due to constraints intrinsic to imaging devices, such as their portability for on-site controls, their reduced cost compared to medical scanners, and their versatility to deal with different inspection configurations. Nonetheless, the need for on-site 3-D imaging is real to improve the characterization of defects with complex morphologies, such as stress corrosion cracks in nuclear plants, or to inspect complex structures with geometries that cannot be considered as 2.5-D. Another main asset of 3-D imaging is to replace the use of mechanical scanners associated with linear arrays when a large volume of the part has to be controlled. Static 3-D imaging with manual positioning could significantly reduce inspection times and costs, but it is crucial that the image computation be fast and the imaged area much wider than the array aperture.

This paper studies reconstruction algorithms to compute 3-D images as fast as possible without resorting to parallel processing and multicore technology. Regarding the set of RF signals to be processed, those contained in the impulse response matrix are not suited for 3-D imaging with matrix arrays [12] because the elements are excited individually, and the large number of transmission/reception sequences considerably reduces volume acquisition rates. In addition, storing the response matrix represents a huge memory load. For example, the formation of 3-D images with a 16×16 matrix imposes to record 256×256 signals of N_t time samples, and the overall volume of data, i.e., $256 \times 256 \times N_t$, is not always recordable by NDT systems due to data transfer limitations.

Manuscript received June 26, 2018; accepted January 16, 2019. Date of publication January 29, 2019; date of current version March 26, 2019. *(Corresponding author: Lucas Merabet.)*

L. Merabet and S. Robert are with the Department of Imaging and Simulation for Nondestructive Testing, CEA-LIST, 91191 Gif-sur-Yvette, France (e-mail: lucas.merabet@cea.fr).

C. Prada is with the Institut Langevin, ESPCI Paris, CNRS, PSL Research University, 75238 Paris, France (e-mail: claire.prada-julia@espci.fr).

Digital Object Identifier 10.1109/TUFFC.2019.2895995

In order to overcome this issue, we propose to form 3-D images with incident plane waves. This technique is widely known in medical imaging to significantly reduce the number of transmissions and, thus, improve volume acquisition rates while decreasing the amount of data to be stored.

Even with plane wave emissions, the post-processing of the RF signals with a "delay-and-sum" algorithm is not sufficient to obtain low computation times for images comprising a large number of voxels, typically between 10^6 and 10^8. This is the reason why, rather than computing the image in the time domain, we propose to investigate imaging algorithms in the wavenumber–frequency (*f-k*) domain, which has been proven to accelerate the computation times. The so-called *f-k* methods are imaging schemes where the image is computed in the Fourier domain by solving an inverse problem and by remapping the wavenumber and frequencies of the RF signals onto the image wavenumber grid. This remapping is specific to the method and usually involves interpolation in the *f-k* domain. They have arisen primarily in seismic migration with the pioneer works of Stolt *et al.* [13], [14] in monostatic imaging. The Stolt formalism describes a passive imaging method where the reflectors in the medium are considered as exploding primary sources. This assumption is valid in an equivalent medium, in the framework of the exploding reflector model (ERM), where the phase velocity is halved to account for the two-way travel time in the physical medium between the transducer array and the reflector. Imaging the reflectors in the region of interest is thus, equivalent to retrieving the acoustic field at the moment $t = 0$ of the explosion, by solving the Helmholtz equation. The Stolt migration was later generalized to multilayered media by Skjelvareid *et al.* [15] to deal with velocity variations along the central axis of the array. Later, Garcia *et al.* [16] adapted the Stolt formalism to 2-D PWI with a modified ERM involving a spatial transformation between the physical and virtual media.

The second approach in imaging in the *f-k* domain is often referred to as the "wavenumber algorithm." It was introduced in the early 1990s in synthetic aperture radar (SAR) with a monostatic measurement setup [17]–[19], and was adapted to deal with bistatic SAR by Callow *et al.* [20]. This method is based on a forward model writing the RF signals in the frequency domain as the convolution of the reflector distribution by the Green's function of the Helmholtz equation. This equation can be inverted by expressing the Green's function as a sum of plane waves via the Weyl identity and gives a representation of the reflector distribution in the wavenumber domain $k_x - k_z$ [21]. More recently, in NDT, Hunter *et al.* [22] followed the same approach as in [20] for the wavenumber algorithm to be used with the inter-element impulse response matrix. In their practical case where 2-D images are calculated with a contact array of 64 elements, they showed that the spatial resolution was improved compared to the TFM imaging in the time domain, and that the computational gain was theoretically of the order of the number of elements. In medical imaging, Moghimirad *et al.* [23] showed that virtual sources can be combined with the wavenumber algorithm to increase the penetration depth of ultrasounds, and thus improve the signal-to-noise ratio compared to the conventional acquisition of the inter-element impulse response matrix. Other methods based on limited diffraction beams were introduced by Lu and Cheng [26], plane waves being a particular case of limited diffraction beams [24], [25].

In this paper, we develop and study 2-D and 3-D reconstruction algorithms in the *f-k* domain to image defects in solids with short computation times. Furthermore, defects are insonified with plane waves to limit the number of data to be processed, thus optimizing the computational performances of the Fourier domain methods. In Section II, we first recall PWI in the time domain. The Lu imaging equation is then derived using an alternative formulation to the limited diffraction beams theory introduced by Lu, following the formalism of the wavenumber algorithm in SAR. Third, the Stolt method for plane wave emissions with linear contact arrays is presented. In Section III, a detailed analysis of the algorithmic complexities is presented, as well as a comparison of the theoretical amplitudes of the PWI, Stolt, and Lu images. The three imaging equations are reformulated with asymptotic expansions of the Fourier integrals in order to highlight the differences in image quality. In Section IV, we generalize the Fourier domain algorithms to immersion testing configurations by extrapolating the acoustic field from the physical array to a virtual array located at the water/steel interface. The quality of 2-D images, the computation times, and the limits of the algorithms are then exhibited and compared for the different methods in a realistic inspection configuration where the region of interest is three times wider than the array aperture. This allows us to assess the capability of the methods to image defects remote from the probe and confirm the theoretical amplitude analysis of Section III, as well as the trends of computational gains. Next, in Section V, we extend the *f-k* algorithms to perform 3-D images with matrix arrays immersed in water, taking into account a plane water/solid interface. To this end, we developed the theory of the ERM underlying the Stolt method for 3-D imaging. The analysis of the image amplitudes is also performed and helps explain why *f-k* methods provide better image quality improvements in 3-D than in 2-D, compared to time-domain PWI. Afterwards, the three methods are evaluated with a steel specimen featuring a distribution of spherical air-filled inclusions. Three-dimensional images of the inclusions are formed in a volume with a base area identical to the matrix array aperture. Finally, this paper ends with experimental images of three crack-type defects with different orientations in a volume five times wider than the array aperture. In this limit case, the number of voxels is larger than 10^7, and we show that the Lu migration provides high-quality 3-D images while reducing the algorithmic complexity and the computation time by a factor of 36.

II. Theoretical Background in 2-D Plane-Wave Imaging

This section sets out the theories in 2-D imaging for a simple case where the array is in contact with a steel block. We first recall the time-domain PWI, which will serve as a reference in terms of image quality and computation time in the sequel. We then present the Lu method, following an SAR approach based

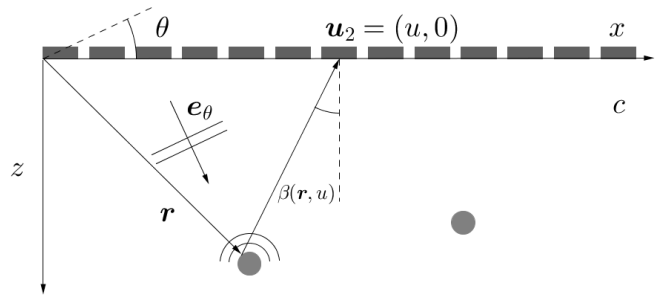

Fig. 1. Geometry and notations used in 2-D imaging with a contact array.

on the Weyl decomposition of the Green's function. Finally, the theory of the Stolt migration as adapted to plane wave emissions by Garcia *et al.* [16] is presented.

A. PWI in the Time Domain

As illustrated in Fig. 1, we consider a transducer array $\mathcal{A}$ with N elements in contact with a homogeneous and isotropic solid medium where longitudinal bulk waves propagate with the phase velocity c. For a concise formalism, it will be assumed that only one type of waves propagates in the solid, with either longitudinal or transverse polarization. The array transmits a plane wave of incidence θ in the medium and records a signal $s_\theta(u, t)$ where u denotes the abscissa of an element and $\mathbf{u}_2 = (u, 0)$ is its position vector. $\beta(\mathbf{r}, u)$ is the backscattering angle from the reflector at $\mathbf{r}$ to the receiver at abscissa u. The medium is assumed to feature a distribution of pointlike reflectors $g(x, z)$. We let $\mathbf{e}_\theta = (\sin\theta, \cos\theta)$ be the unit normal vector to the plane wavefront, and by convention, the leftmost element will be chosen as the origin of the coordinate system. Here, we briefly present the imaging method in the time domain for NDT systems [8]. Compared to the medical PWI where the beamforming process is performed "line by line" with a subset of several adjacent receivers, images in NDT are formed "point by point" by focusing in receive mode with the whole aperture. Let us consider a point $\mathbf{r}$ of coordinates (x, z) in the medium. The arrival time of the plane wavefront at position $\mathbf{r}$ is

$$t_e(\mathbf{r}, \theta) = \frac{\mathbf{r} \cdot \mathbf{e}_\theta}{c} + \tau_e(\theta) \tag{1}$$

where $\tau_e(\theta)$ is the emission delay of the leftmost transducer element. The time of flight of the backscattered wave from $\mathbf{r}$ to the receiver at u is

$$t_r(\mathbf{r}, u) = \frac{\|\mathbf{r} - \mathbf{u}_2\|}{c}. \tag{2}$$

Finally, if steered plane waves of angles $\theta \in \Theta$ are transmitted, a compounded image $i(\mathbf{r})$ can be formed by summing coherently all the RF signals recorded with the N elements at arrival times $t_e(\mathbf{r}, \theta) + t_r(\mathbf{r}, u)$:

$$i(\mathbf{r}) = \left| \sum_{\theta \in \Theta} \sum_{u \in \mathcal{A}} s_\theta \left(u, t_e(\mathbf{r}, \theta) + t_r(\mathbf{r}, u)\right) \right|. \tag{3}$$

The algorithmic complexity of time-domain PWI, i.e., the number of operations to form an image, can be deduced from (3). Q will denote the number of plane waves, N the number of elements, and $N_x N_z$ the number of pixels. In imaging systems, delay laws and times of flight are precalculated and stored in memories, and only the image reconstruction (4) is done in real time. To do so, each RF signal $s_\theta(u, t)$ needs to be linearly interpolated to extract the amplitude $s_\theta(u, t_e + t_r)$, which accounts for four operations (two additions and two multiplications) per pixel, angle and receiver. Hence, the algorithmic complexity $\mathcal{C}_P$ of time-domain PWI is given by

$$C_P = 4QNN_xN_z. \tag{4}$$

Throughout this paper, the above algorithmic complexity will serve as a reference to quantify the gains in computation time. We now go on to the theories of *f-k* methods.

B. Lu f-k Method

Hereafter, we derive the Lu method for plane wave emissions using a forward model and the formalism described in [19] for bistatic imaging SAR. It consists in writing a forward model linking the recorded signal to the distribution of scatterers in the medium. In the sequel, $k_u - \omega$ will denote the wavenumber domain of the RF signals and $k_x - k_z$ the frequency domain of the image. Lowercase letter will be used for space and space–time domain signals, capital letters otherwise. The following definition is adopted for Fourier transforms:

$$s_\theta(u, t) = \iint S_\theta(k_u, \omega) e^{i(k_u u + \omega t)} dk_u d\omega. \tag{5}$$

Assuming that there is no attenuation and that the element radiation patterns are omnidirectional, the forward propagation model for a single plane wave with incidence angle θ and wave vector $\mathbf{k}_\theta = k\mathbf{e}_\theta$ is [4]

$$S_\theta(u, \omega) = A(\omega) \iint e^{-i\mathbf{k}_\theta \cdot \mathbf{r}} g(\mathbf{r}) H_0^{(2)}(k\|\mathbf{u}_2 - \mathbf{r}\|) dx dz \tag{6}$$

where $A(\omega)$ is the emission spectrum and $H_0^{(2)}$ is the Hankel function of the second kind. Equation (6) is valid for large transducer arrays where edge diffraction effects can be neglected (otherwise, an apodization function can be used in transmit mode), and it expresses the back-and-forth wave propagation in the medium with incident plane waves and backscattered cylindrical waves. The aim now is to invert this equation to retrieve $g(\mathbf{r})$. To do so, $H_0^{(2)}$ is decomposed in terms of plane waves using the Weyl identity [8]

$$H_0^{(2)}(k\|\mathbf{u}_2 - \mathbf{r}\|) = \int \frac{e^{ik_u(u-x) - iz\sqrt{k^2 - k_u^2}}}{\sqrt{k^2 - k_u^2}} dk_u. \tag{7}$$

Injecting (7) in (6) allows to write $S_\theta(u, \omega)$ as

$$\begin{aligned} S_\theta(u, \omega) &= A(\omega) \int \frac{e^{ik_u u}}{\sqrt{k^2 - k_u^2}} \\ &\quad \times \left(\iint g(\mathbf{r}) e^{-i(k_u + k\sin\theta)x - iz(k\cos\theta + \sqrt{k^2 - k_u^2})} dx dz \right) dk_u \end{aligned} \tag{8}$$

and taking the lateral Fourier transform of (8) yields

$$S_\theta(k_u,\omega) = A(\omega)\frac{G\left(k_u + k\sin\theta, \sqrt{k^2-k_u^2} + k\cos\theta\right)}{\sqrt{k^2-k_u^2}} \tag{9}$$

and finally, the 2-D Fourier transform $G(k_x,k_z)$ of $g(x,z)$ is

$$G(k_x,k_z) = \frac{\sqrt{k^2-k_u^2}}{A(\omega)} S_\theta(k_u,\omega) \tag{10}$$

with

$$\begin{cases} k_u = k_x - k\sin\theta \\ k = \dfrac{k_x^2+k_z^2}{2k_x\sin\theta + 2k_z\cos\theta}. \end{cases} \tag{11}$$

Equation (10) gives an explicit relationship between the spectrum of the reflector distribution $G(k_x,k_z)$ and the spectrum of the recorded signal $S(k_u,\omega)$, and translates the fact that S_θ needs to be remapped, or in other words resampled, on the grid $(k_u(k_x,k_z), k(k_x,k_z))$. Implementationwise, this step consists in interpolating the signal on to a new grid through a 2-D interpolation. Theoretically, with the hypotheses mentioned above, (10) and (11) provide the same result G for each transmission angle θ. In practice, due to the limited aperture and the spatial sampling of the array, each emission gives an estimation G_θ of G and a high-quality image is obtained by coherently summing the distributions $G_\theta, \theta \in \Theta$ obtained with several emissions and taking the inverse Fourier transform of this sum:

$$g(x,z) = \left| \mathcal{F}^{-1}_{k_x,k_z}\left\{ \sum_{\theta\in\Theta} G_\theta(k_x,k_z) \right\} \right|. \tag{12}$$

C. Stolt f-k Migration

The Stolt *f-k* migration was first introduced in 1978 for pulse-echo seismic imaging. The formalism describes a passive detection technique where the reflectors in the medium are considered as primary sources. This assumption can be made thanks to the so-called ERM: there exists a virtual medium $(\hat{c},\hat{x},\hat{z})$ where all the reflectors explode in concert at $t=0$, acting as primary sources, and the resulting acoustic field at the array location is the same as that recorded in the physical medium (c,x,z). The passive imaging method is derived in Section II-C1, and in the second step, the ERM associated with plane wave emissions is described.

1) Passive Imaging in the Virtual Medium: We assume here a medium of celerity $\hat{c}$ featuring pointlike sources exploding at $t=0$, and we will explain later how we can get back to a configuration where this assumption can be made. The explosion generates an acoustic field $\phi(x,z,t)$ in the medium, and an infinite array at the surface of the medium records a signal $s(x,t)$. Imaging the exploding sources is thus equivalent to retrieving the wavefield $\phi(x,z,t=0) = g(x,z)$ from the acquired data $\phi(x,z=0,t) = s(x,t)$. We will consider in the sequel that only upward waves propagate, which allows to extrapolate the wavefield from the array to any depth $z>0$. Let us first write $\phi(x,z,t)$ as

$$\phi(x,z,t) = \iint \Phi(k_x,z,\omega) e^{i(k_x x+\omega t)} dk_x d\omega. \tag{13}$$

Because ϕ solves the wave equation, $\Phi(k_x,z,\omega)$ is solution of the Helmholtz equation:

$$\frac{\partial^2\Phi}{\partial z^2} + k_z^2\Phi = 0 \tag{14}$$

with the dispersion equation

$$k_z^2 = \frac{\omega^2}{\hat{c}^2} - k_x^2. \tag{15}$$

Now, with the assumption that only upward going waves are propagating, $\Phi(k_x,z,\omega)$ at an arbitrary depth z can be calculated from the knowledge of the field at at the array location $z=0$, leading to

$$\Phi(k_x,z,\omega) = S(k_x,\omega)e^{ik_z z}. \tag{16}$$

Then, injecting (16) in (13) at $t=0$ yields an expression of the acoustic field at start time

$$\phi(x,z,t=0) = \iint S(k_x,\omega) e^{i(k_x x+k_z z)} dk_x d\omega. \tag{17}$$

Equation (17) describes a nonuniform Fourier transform. We can go further and rewrite it as a uniform Fourier transform by letting

$$\omega(k_x,k_z) = \hat{c}\ \mathrm{sign}(k_z)\sqrt{k_x^2+k_z^2}. \tag{18}$$

Finally, ϕ can be expressed as an inverse uniform Fourier transform

$$\phi(x,z,0) = \iint S(k_x,\omega(k_x,k_z)) e^{i(k_x x+k_z z)} \frac{\hat{c}k_z}{\sqrt{k_x^2+k_z^2}} dk_x dk_z \tag{19}$$

and the exploding reflector distribution can be expressed in the (k_x,k_z) domain as

$$\hat{G}(k_x,k_z) = \frac{\hat{c}k_z}{\sqrt{k_x^2+k_z^2}} S(k_x,\omega(k_x,k_z)). \tag{20}$$

$\hat{g}(x,z)$ is finally obtained by taking the total inverse Fourier transform of $\hat{G}(k_x,k_z)$.

2) Equivalence Between the Physical and the Virtual Media: In this paragraph, the 2-D spatial transformation linking the virtual and physical media is presented. It is derived from that of Garcia *et al.* [16] and will be generalized to matrix arrays in Section V. Instead of finding a transformation giving an exact adequation between wave arrival times, the following linear transformation is considered:

$$\begin{cases} \hat{c} = \alpha_\theta c \\ \hat{x} = x + \gamma_\theta z \\ \hat{z} = \beta_\theta z. \end{cases} \tag{21}$$

The spatial transformation in (21) can be expressed as $\hat{\mathbf{r}} = \mathbf{r}\mathbf{T}$, where

$$\mathbf{T} = \begin{pmatrix} 1 & 0 \\ \gamma_\theta & \beta_\theta \end{pmatrix}. \tag{22}$$

It should be noted that the array is invariant by $\mathbf{T}$, which is desired. For each plane wave emission, the ERM definition

requires to correct the arrival time $t_e(\mathbf{r},\theta) + t_r(\mathbf{r},u)$ with reception delays, that is,

$$\tau_{\mathbf{r}}(u) = t_e(\mathbf{r},\theta) + t_r(\mathbf{r},u) - \frac{u\sin\theta}{c}. \tag{23}$$

The reception delay $-u\sin\theta/c$ allows for diffraction hyperbolae of two reflectors located at the same depth to be horizontally aligned on the B-scan. This is equivalent to considering that the field at $z = 0$ generated by the explosion is

$$S(u,\omega) = S_\theta(u,\omega)e^{iku\sin\theta}. \tag{24}$$

With $\mathbf{e}_\theta = (\sin\theta, \cos\theta)$, $\tau_{\mathbf{r}}(u)$ can be rewritten as

$$\tau_{\mathbf{r}}(u) = \frac{1}{c}\left[(\mathbf{r}-\mathbf{u}_2)\cdot\mathbf{e}_\theta + \|\mathbf{r}-\mathbf{u}_2\|\right]. \tag{25}$$

The corresponding arrival time in the virtual medium is

$$\hat{\tau}_{\mathbf{r}}(u) = \frac{1}{\hat{c}}\|\hat{\mathbf{r}}-\mathbf{u}_2\| = \frac{1}{\hat{c}}\|(\mathbf{r}-\mathbf{u}_2)\mathbf{T}\| \tag{26}$$

and finally the arrival-time difference between both media is

$$W_{\mathbf{r}}(u) = \hat{\tau}_{\mathbf{r}}(u) - \tau_{\mathbf{r}}(u). \tag{27}$$

Since most of the acoustic energy is concentrated around the apex of the diffraction hyperbola, the transformation in (22) has to satisfy $W_{\mathbf{r}}(u) = 0$ at the highest order possible around $u = x$. Writing the second-order Taylor expansion of $W_{\mathbf{r}}(u)$ at $u = x$ and imposing the nullity of the derivatives of order up to two yields a system of three equations and three unknowns and ensures that $W_{\mathbf{r}}(u) = \mathcal{O}(x-u)^3$ around $u = x$. The resolution of the system provides the coefficients of the linear transformation in (22)

$$\begin{cases} \alpha_\theta = \dfrac{1}{\sqrt{1+\cos\theta+\sin^2\theta}} \\ \beta_\theta = \dfrac{\sqrt{1+\cos\theta}}{2-\cos\theta} \\ \gamma_\theta = \dfrac{\sin\theta}{2-\cos\theta}. \end{cases} \tag{28}$$

The principle of the ERM is to fit the depths and excentricities of the diffraction hyperbolae in both media by adjusting the above coefficients for every incidence angle θ. This gives a very good fit near the apex, but the arrival-time errors diverge when $x - u \to \pm\infty$. Finally, the image for a steering angle θ in the physical medium is

$$g(x,z) = \hat{g}_\theta(x+\gamma_\theta z, \beta_\theta z) \tag{29}$$

where $\hat{g}_\theta(x,z)$ is deduced from the measured signal S_θ with (20), that is,

$$g(x,z) = \mathcal{F}_{k_x}^{-1}\left\{e^{ik_x\gamma_\theta z}\mathcal{F}_{k_z}^{-1}\left[\hat{G}_\theta\left(k_x, \frac{k_z}{\beta_\theta}\right)\right]\right\}. \tag{30}$$

The final compounded image is formed by summing the individual images for all the steering angles θ, that is,

$$g(x,z) = \mathcal{F}_{k_x}^{-1}\left\{\sum_{\theta\in\Theta} e^{ik_x\gamma_\theta z}\mathcal{F}_{k_z}^{-1}\left[\hat{G}_\theta\left(k_x, \frac{k_z}{\beta_\theta}\right)\right]\right\}. \tag{31}$$

In (31), an inverse Fourier transform with respect to z is performed for each steering angle in order to compound the images formed in the physical medium. It should be noted that the images formed in the exploding reflector (ER) medium cannot be coherently summed because the properties of this medium depend on θ.

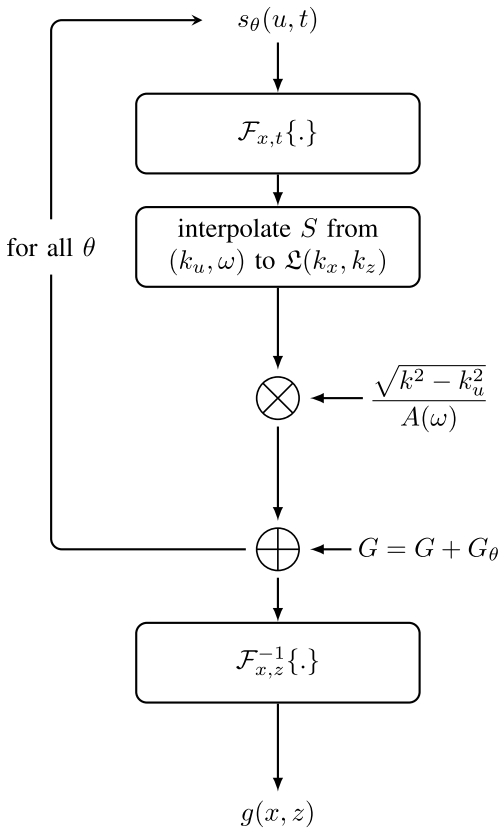

Fig. 2. Steps involved in the implementation of the Lu method: 1) the signal $s_\theta(u,t)$ is 2-D Fourier transformed in $S_\theta(k_u,\omega)$; 2) $S_\theta(k_u,\omega)$ is interpolated on the frequency grid $\mathfrak{L}(k_x,k_z)$; and 3) the interpolated signal is multiplied by $(k^2-k_u^2)^{1/2}/A(\omega)$. Step 1)–3) are repeated for all angles and the individual images $G_\theta(k_x,k_z)$ are summed together. Finally, a single 2-D inverse Fourier transform is performed on $G(k_x,k_z)$ to obtain the compounded image $g(x,z)$.

III. Theoretical Analysis of the Computational and Graphic Performances

This section first gives the algorithmic complexities of the three methods to estimate the gains in computation time. Then the imaging equations are reformulated with asymptotic expansions of the Fourier integrals to interpret the differences between the image amplitudes.

A. Algorithmic Complexities of the f-k Methods

The synoptic diagram shown in Fig. 2 describes the steps involved in the image reconstruction with the Lu method. In the following, d denotes the array pitch, N the number of elements, Q the number of steering angles, N_t the number of time samples, and f_s is the sampling rate. Likewise, L_x and L_z will denote the width and height of the image, and N_x and N_z the number of pixels along the lateral and axial directions. The wavenumber–frequency sample grid (k_u,ω) is defined by $k_u = (2\pi/Nd)\cdot[-N/2+1,\ldots,N/2]$ and $\omega = (2\pi f_s/N_t)\cdot[0,\ldots,N_t/2]$, and the image wavenumber grid (k_x,k_z) is defined by $k_x = (2\pi/L_x)\cdot[-N_x/2+1,\ldots,N_x/2]$ and $k_z = (2\pi/L_z)\cdot[0,\ldots,N_z/2]$.

TABLE I
COMPUTATION STEPS AND ALGORITHMIC COMPLEXITIES IN THE LU AND STOLT METHODS

Steps	Complexities for Lu	Complexities for Stolt
$\mathcal{F}_{x,t}\{.\}$	$QNN_t\log_2(NN_t)$	$QNN_t\log_2(NN_t)$
2D interp.	$12QN_xN_z$	$12QN_xN_z$
$\mathcal{F}_{x,z}^{-1}\{.\}$	$N_xN_z\log_2(N_xN_z)$	-
$\mathcal{F}_{z}^{-1}\{.\}$	-	$QN_xN_z\log_2(N_z)$
$\mathcal{F}_{x}^{-1}\{.\}$	-	$N_xN_z\log_2(N_x)$

Zero padding is applied to the signals in the axial and lateral directions before performing the fast Fourier transform (FFT) in order to improve the accuracy of the bilinear interoplator used to map S_θ from (k_u,ω) to $\mathfrak{L}(k_x,k_z)$, where

$$\mathfrak{L}:(k_x,k_z)\mapsto\left(k_x-k\sin\theta,\frac{k_x^2+k_z^2}{2k_x\sin\theta+2k_z\cos\theta}\right) \quad (32)$$

denotes the *f-k* domain resampling mapping. The complexities of the computational steps are summed up in Table I. We also considered the fact that a bilinear interpolation requires six additions and six multiplications for every interpolated point. This interpolation deals with complex numbers, thus each interpolated point requires 24 elementary operations. However, in consideration of the symmetry of the Fourier spectrum, the interpolation is only performed on half of the signal spectrum. Therefore, the global complexity of the Lu algorithm is

$$\mathcal{C}_L\approx QNN_t\log_2(NN_t)+12QN_xN_z+N_xN_z\log_2(N_xN_z). \quad (33)$$

The complexity $\mathcal{C}_P$ of time-domain PWI is given in (4), and the ratio between $\mathcal{C}_P$ and $\mathcal{C}_L$ takes the form

$$\frac{\mathcal{C}_P}{\mathcal{C}_L}\approx\frac{4N}{12+\frac{\log_2(N_xN_z)}{Q}+\frac{NN_t\log_2(NN_t)}{N_xN_z}}. \quad (34)$$

The Stolt algorithm follows the steps presented in Fig. 3. S_θ is interpolated from the sample grid (k_u,ω) to a new grid $\mathfrak{S}(k_x,k_z)$ defined by

$$\mathfrak{S}:(k_x,k_z)\mapsto\left(k_x,\hat{c}\ \mathrm{sign}(k_z)\sqrt{k_x^2+\left(\frac{k_z}{\beta}\right)^2}\right). \quad (35)$$

Contrary to the Lu algorithm, an inverse Fourier transform in the z direction is performed for every angle. This accounts for $QN_xN_z\log_2(N_z)$ operations. In practice $Q\gg1$, and the algorithmic complexity of the Stolt migration adds up to

$$\mathcal{C}_S\approx QNN_t\log_2(NN_t)+12QN_xN_z+QN_xN_z\log_2(N_z) \quad (36)$$

and the computational gain of the Stolt method over PWI when $N_x\gg N$ is given by the ratio

$$\frac{\mathcal{C}_P}{\mathcal{C}_S}\sim\frac{4N}{12+\log_2(N_z)}. \quad (37)$$

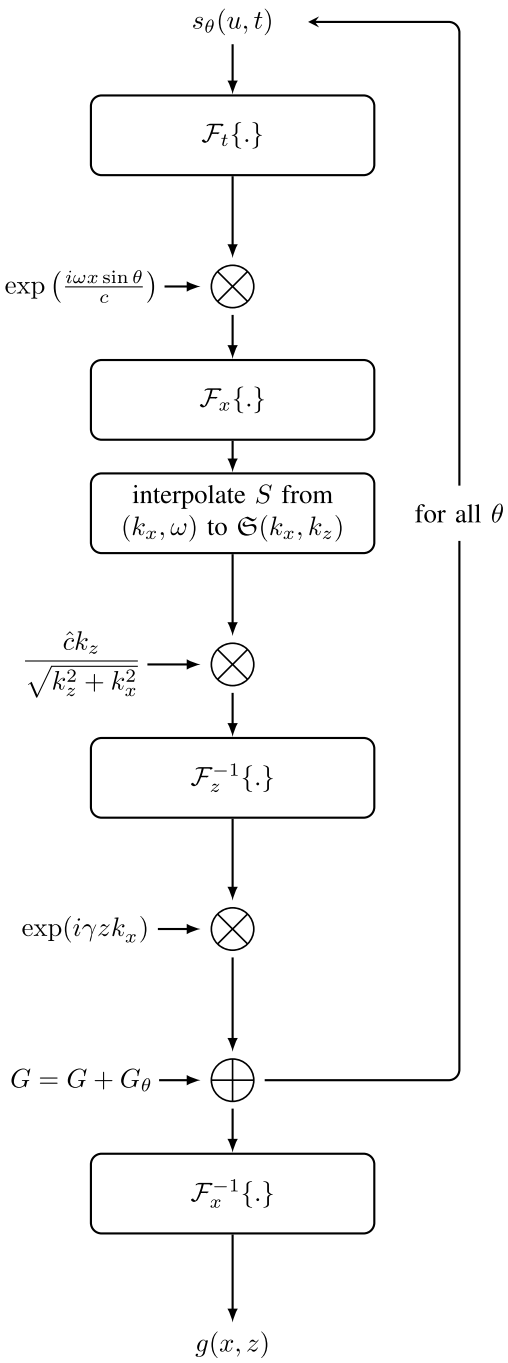

Fig. 3. Steps involved in the implementation of the Stolt migration: 1) the signal $s_\theta(u,t)$ is 1-D Fourier transformed in $S_\theta(u,\omega)$; 2) emission delays are substracted (aligning the diffraction hyperbolae); 3) $S_\theta(u,\omega)$ is Fourier transformed in the x direction, yielding $S_\theta(k_u,\omega)$; 4) $S_\theta(k_u,\omega)$ is interpolated on the frequency grid $\mathfrak{S}(k_x,k_z)$; 5) the interpolated signal is multiplied by $\hat{c}k_z/(k_z^2+k_x^2)^{1/2}$; 6) and 7) the signal is inverse Fourier transformed in z and passed from the coordinates $\hat{x}$ to x. Steps 1)–7) are repeated for all angles and the individual images $G_\theta(k_x,k_z)$ are summed. Finally, a single inverse Fourier transform is performed on $G(k_x,k_z)$ to obtain the compounded image $g(x,z)$.

For a 2-D image with $N_xN_z\geq10^5$ pixels, $N_t=1024$, $N\leq128$ and $Q\geq20$, Q and $\log_2(N_xN_z)$ are of the same order of magnitude, as well as $NN_t\log_2(NN_t)$ and N_xN_z. In that case, it is expected that

$$\frac{\mathcal{C}_P}{\mathcal{C}_L}\sim\frac{N}{3}\quad\text{and}\quad\frac{\mathcal{C}_P}{\mathcal{C}_S}\sim\frac{2N}{11} \quad (38)$$

B. Physical Interpretation of the Imaging Equations

In Section IV, we will emphasize that the images given by the three algorithms (time-domain PWI, Stolt and Lu) differ in quality. In order to better interpret these differences, the imaging equations are reformulated below as continuous sums over the receivers and frequencies. This type of analysis has been carried out in [27] to compare the pulse-echo Stolt method to the synthetic aperture focus transmit technique, and in [28] to compare the TFM with the wavenumber algorithm [22]. On the other hand, for clarity, it is assumed that the medium is insonified by a single plane wave. Noting $K(\mathbf{r},u,\omega) = S(u,\omega)e^{ik(\mathbf{r}.\mathbf{e}_\theta+\|\mathbf{u}_2-\mathbf{r}\|)}$, the amplitude of the PWI image at a point located at $\mathbf{r}=(x,z)$ is

$$g_P(\mathbf{r}) = \iint K(\mathbf{r},u,\omega)\,du d\omega. \tag{39}$$

It is demonstrated in Appendix A that similar expressions can be found for the *f-k* methods provided that kz is sufficiently large for all frequencies in the signal bandwidth. Under this assumption, the image amplitude at $\mathbf{r}$ for the Lu method can be written as

$$\frac{g_L(\mathbf{r})}{\sqrt{2i\pi}} \approx \iint \frac{k^{3/2}\cos^2\beta(\mathbf{r},u)}{\|\mathbf{r}-\mathbf{u}_2\|^{1/2}} K(\mathbf{r},u,\omega) du d\omega \tag{40}$$

where $\beta(\mathbf{r},u) = \arccos(z/\|\mathbf{r}-\mathbf{u}_2\|)$ is the backscattering angle from the point located at $\mathbf{r}$ to the receiver of abscissa u (see Fig. 1). Compared to PWI, $K(\mathbf{r},u,\omega)$ is multiplied by a weighting function acting as a filter in space and frequency. What can be deduced from (40) is that the Lu method penalizes defects at high angles with respect to the array, as well as defects located at large depths. The $k^{3/2}$ term is a high-pass filter that shifts up the center frequency of the RF signals and narrows down the bandwidth, which is expected to improve the lateral resolution and slightly degrade the axial resolution. Similarly, for the Stolt method, the amplitude $g_S(\mathbf{r})$ can be expressed as

$$\frac{g_S(\mathbf{r})}{\sqrt{2i\pi}} \approx \iint \frac{\hat{k}^{1/2}\cos\beta(\hat{\mathbf{r}},u)}{\|\hat{\mathbf{r}}-\mathbf{u}_2\|^{1/2}} e^{i\omega W_{\mathbf{r}}(u)} K(\mathbf{r},u,\omega) du d\omega \tag{41}$$

where $W_{\mathbf{r}}(u)$ is the arrival-time error in the ERM defined in (27). Compared to the Lu imaging equation, a similar weighting function is obtained in space, but features $\hat{\mathbf{r}}$ instead of $\mathbf{r}$, because the Stolt method forms the image in the ERM medium. It is to be noticed that amplitudes at high angles are penalized by the $\cos\beta(\hat{\mathbf{r}},u)$ factor instead of $\cos^2\beta(\mathbf{r},u)$ for the Lu method, and the high-pass filter now is defined by $k^{1/2}$, having less effects on the spectral content of the RF signals. The $e^{i\omega W_{\mathbf{r}}(u)}$ term is close to 1 when $u \sim x$ and oscillates rapidly with respect to ω when $|x-u|$ increases. For a point located outside of the array aperture, the value of $|x-u|$ is large for all the receivers, and the sum of signals in (41) is not coherent. As a result, the Stolt method is expected to perform poorly when forming images much larger than the aperture, which is often the case in NDT.

IV. Generalization and Application of the 2-D Imaging Methods to Immersion Arrays

Previously, the theories have been introduced with an inspection configuration where the transducer array is directly in contact with the specimen. Industrial inspections are rather carried out in water-filled tanks or by equipping probes with Plexiglas wedges. The goal is to prevent the array elements from being damaged on rough surfaces and to inspect specimens with complex geometries. As an example, the *f-k* imaging methods are developed in the sequel for an immersion probe and a specimen with a planar surface. As described in Fig. 4, a linear array of N elements is facing a steel block with a water column height denoted by h. Ultrasonic waves propagate with the phase velocities c_1 in water and c_2 in the specimen (with $c_2 > c_1$). A plane wave of angle θ_1 is transmitted in the first medium, then refracted as a plane wave of angle $\theta_2 = \arcsin((c_2/c_1)\sin\theta_1)$ in the second medium. We now propose two extrapolation methods adapted to the Stolt and Lu methods. To this end, the transmission coefficients are assumed to be equal to 1, and, as previously, the diffraction by the array edges is neglected by considering an infinite aperture.

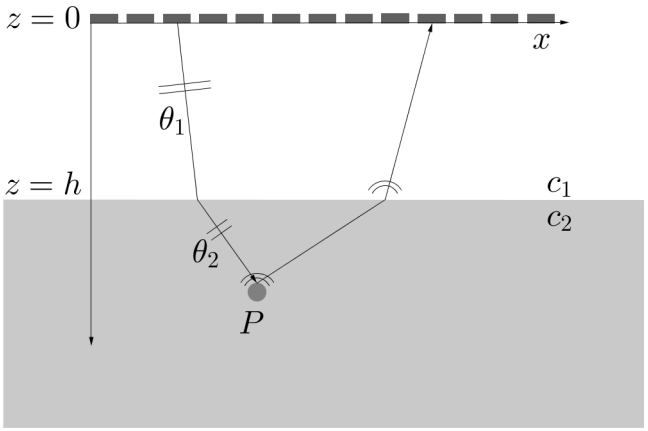

Fig. 4. Two-dimensional imaging with a linear array immersed in water and located at a distance h from the steel specimen. The plane wave of incidence angle θ_1 is refracted by the water/steel interface and propagates in the solid with the angle θ_2.

A. 2-D f-k Migrations Under a Plane Water/Steel Interface

1) Stolt f-k Migration: It follows from (16) that, as long as the celerity remains constant, the wave field can be extrapolated from depth z to depth $z' > z$. Applying this property in the first medium, we deduce that the wavefield at the interface $z=h$ in the ERM medium 1 is given by

$$\hat{\Phi}(k_x,h,\omega) = \hat{\Phi}(k_x,0,\omega)\exp\left(ik_z^1 h\right) \tag{42}$$

where

$$k_z^1 = \sqrt{\left(\frac{\omega}{\hat{c}_1}\right)^2 - k_x^2} \tag{43}$$

and $\hat{c}_1 = \alpha_1\, c_1$ is the phase velocity in the ERM medium 1 for a single plane wave of incidence angle θ_1. Then, getting back in the physical medium, we obtain the wavefield at $z=h$

$$\Phi(k_x,h,\omega) = \Phi(k_x,0,\omega)\exp\left[ih\left(\beta_1 k_z^1 + \gamma_1 k_x\right)\right] \tag{44}$$

where β_1 and γ_1 are the coefficients defining the spatial transformation in (22). Once the wavefield is known at the interface,

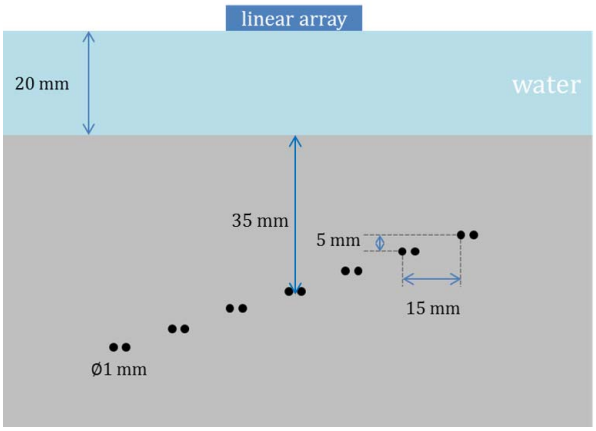

Fig. 5. Inspection testing configuration used for the simulation of echoes: a linear array is immersed in water over a steel block of 60-mm thickness featuring a series of seven pairs of side-drilled holes of 1-mm diameter. The center-to-center distance between two holes is of 2 mm. The region of interest is four times wider than the array aperture.

it is possible to apply the Stolt algorithm in the second medium to form the final image.

2) Lu Method: The principle of the Lu method for immersion arrays is to consider a virtual array located at the interface $z = h$ that transmits a plane wave of angle θ_2 into the solid. The array is assumed infinite and the angular dependency of the transmission coefficient is neglected, which is possible provided that the incidence angle θ_1 remains small. In that case, noting $S_{\theta_1}(k_x, \omega)$ the signal recorded by the physical array, and $k_1 = \omega/c_1$, the signal $S_{\theta_2}(k_x, \omega)$ recorded by the virtual array writes

$$S_{\theta_2}(k_x, \omega) = S_{\theta_1}(k_x, \omega) e^{ih\left(k_1 \cos\theta_1 + \sqrt{k_1^2 - k_x^2}\right)}. \tag{45}$$

The $e^{ihk_1 \cos\theta_1}$ propagation term accounts for the fact that the virtual array emits at depth h with regard to the physical array, while $e^{ih(k_1^2 - k_x^2)^{1/2}}$ accounts for the downward extrapolation of the wavefield. The Lu algorithm can then be performed without modification to image the solid medium by replacing the measured wavefield at $z = 0$ by that recorded with the virtual array at $z = h$.

It should be noted that the principle of wavefield extrapolation for both Fourier domain algorithms requires a multiplication of the received signal spectrum by a complex exponential. The cost of this operation is, therefore, negligible compared to the other steps and the algorithmic complexities previously described for contact arrays still hold. As far as time-domain PWI is concerned, the times of flight $t_r(\mathbf{r}, u)$ in (2) associated with backscattered waves are computed using the Fermat principle and the Newton method to find the points of the water/steel interface that minimize the propagation times [8].

B. Evaluation of the 2-D Imaging Methods With Simulated Data

Time-domain PWI, the Stolt migration, and the Lu method were implemented and optimized in MATLAB (MathWorks, Natick, MA) and tested on a set of simulated data. The inspected medium in Fig. 5 is a steel block featuring a series of seven pairs of side-drilled holes of 1-mm diameter.

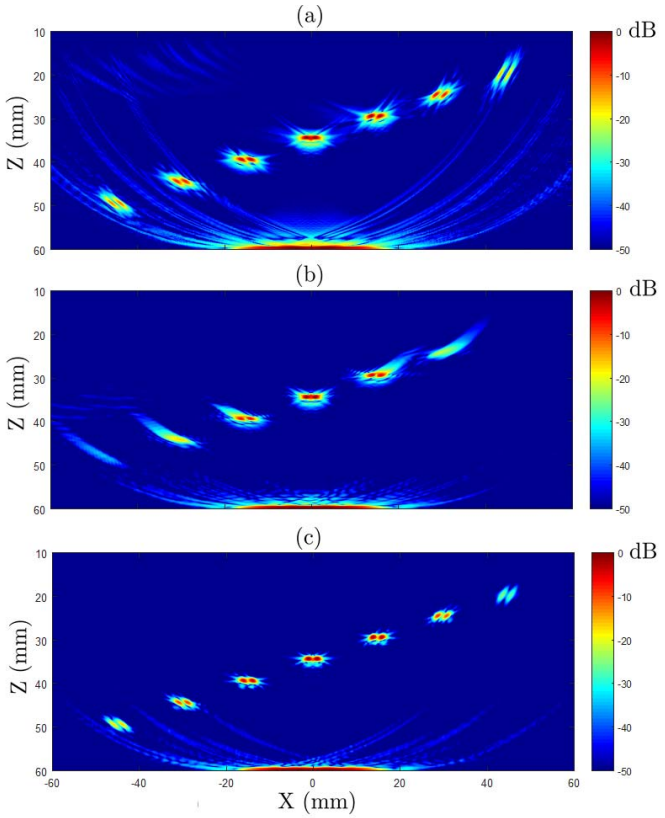

Fig. 6. Images computed by post-processing simulated signals with (a) time-domain PWI, (b) the Stolt migration, and (c) the Lu method. For each image, the reference amplitude (0 dB) corresponds to the pair of holes located on the vertical central axis of the array.

The center-to-center distance for each pair of holes is 2 mm. Longitudinal waves propagate in the solid with the phase velocity $c = 5.9$ mm $\cdot\ \mu s^{-1}$, while transverse waves are not considered in the simulation. The linear array is composed of 64 elements with a pitch of 0.6 mm and is immersed in water at $h = 20$ mm above the specimen. Elements are excited by a Gaussian signal with a center frequency of 5 MHz and a bandwidth of 80% at -6 dB. Since the region to be imaged is much wider than the array aperture (i.e., more than three times wider than the aperture), the number of plane waves has to be large to produce a high-quality image. Thus, the series of flaws is insonified by 141 plane waves propagating from $-70°$ to $70°$ with an angular step of $1°$. The signals were simulated using the CIVA software (CEA-LIST, Gif-sur-Yvette, France) [29], [30]. The codes were run on an Intel Xeon 3.30-GHz CPU and 16 GB of RAM. The images provided by the three reconstruction algorithms are displayed in Fig. 6. For each of them, the reference amplitude (0 dB) corresponds to the maximum amplitude of the defect echoes, i.e., the echoes of the pair of holes at $x = 0$. It should be noted that the quality of images could be slightly improved with apodizations in transmit mode to limit the effects of side lobes and the diffraction by the array edges. Though, our images are sufficiently satisfactory to draw clear conclusions about the three methods. In NDT, since most acquisition systems do not allow to excite elements in parallel with electric signals of different amplitudes, an alternative solution that

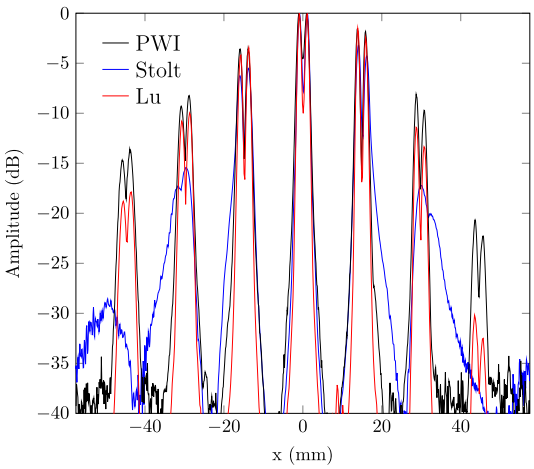

Fig. 7. Variation of the maximum amplitude of echoes along the x-direction.

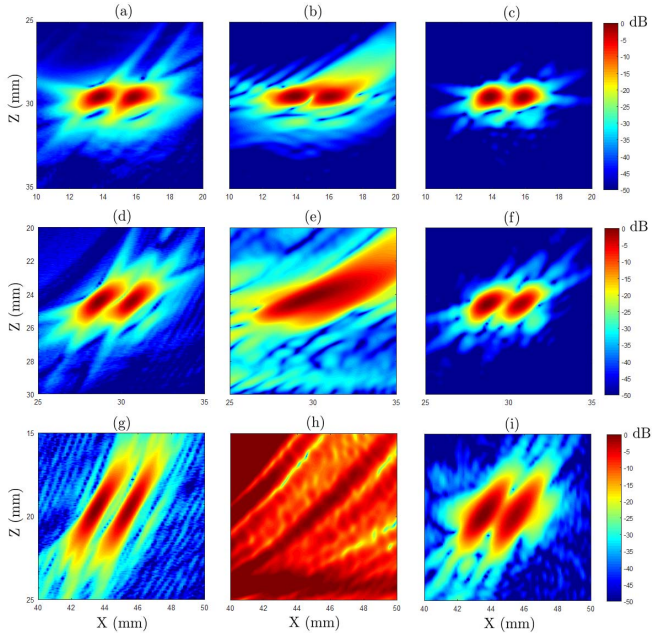

Fig. 8. Close-ups around the three rightmost pairs displayed in decibels, where the reference amplitude is the maximum amplitude of the pair considered. (a), (d), and (g) PWI. (b), (e), and (h) Stolt. (c), (f), and (i) Lu.

partially addresses this issue consists in apodization factors in receive mode with the radiation beam patterns of the array elements [31]. In the present case where a water/steel interface is considered, the interface transmission coefficients must also be considered in the imaging equations, which increase the computation times with no substantial improvement in the quality of images. In NDT, the weighting factors are rather useful in imaging with transverse waves and in multimodal imaging to avoid imaging artifacts related to interface echoes [32], [33].

At a depth of 60 mm, it can be observed that the amplitude of the back-wall echo decreases with the *f-k* methods, which is in agreement with our theoretical analysis of the image amplitudes in Section III-B. Qualitatively, it is clear that the Lu method offers an image quality close to that of time-domain PWI in the absence of noise, whereas the Stolt image is not fully satisfactory everywhere in the region of interest. For more quantitative analysis, the three X-echodynamic curves are superimposed in Fig. 7. Each one represents the variation of the maximum amplitude of echoes according to the x-direction, after removing the back-wall echo. As predicted by the theory, the comparison of the X-echodynamic curves confirms that the Fourier-domain methods improve the lateral resolution compared to time-domain PWI provided that the reflectors are located under the array aperture. Beyond the aperture, i.e., for $|X| > 19.2$ mm, higher damping of echoes is observed at high angles for the Lu method compared to PWI, which can potentially impair the capability of the method to detect defects at high angles in the presence of electronic or structural noise. For instance, for the pair of holes at $x = 45$ mm corresponding to the highest angle, we can notice a significant amplitude difference of 8 dB between the PWI and Lu images.

Regarding the Stolt image, the defect echoes outside of the array aperture are either blurry (pairs at $x = -45, -30$, and 30 mm) or missing ($x = 45$ mm). This is due to arrival-time errors in the ERM which amount to summing amplitudes of the wrong diffraction hyperbolae. This corroborates the theoretical analysis in Section III-B and confirms that the Stolt method is unsuitable for imaging defects outside of the array aperture. The close-ups in Fig. 8 around the three rightmost pairs of side-drilled holes highlight that the Lu methods provide a slightly better lateral resolution than PWI, and a slightly worse axial resolution. It also shows that the Stolt method is able to separate the defects under the aperture but the echoes outside of the aperture are first blurry, then missing.

Finally, the execution times measured using the "tic" and "toc" MATLAB functions are indicated in Fig. 9, along with plots of the algorithmic complexities (4), (33), and (36). For both frequency algorithms, the "tic" function was placed just before the first direct FFT of the RF signals, and "toc" immediately after the inverse FFT (cf. Figs. 2 and 3). For PWI, the computation of propagation times with (1) and (2) precedes the "tic" and "toc" calls, and only the reconstruction time was measured. Each curve in Fig. 9 gives the evolution of the computation times for a number of pixels ranging from 10^4 to 5.10^6. When the number of pixels is larger than 10^6, the computation times linearly increase for the three methods [cf. Fig. 9(b)], which is also the case for the algorithmic complexities [cf. Fig. 9(a)], meaning that the interpolation step becomes preponderant. For a high number of pixels, the Stolt migration shows a numerical gain up to 12 compared to PWI, and the Lu method is up to 24 times faster than PWI. In comparison, the algorithmic complexities in Section III-A for $N = 64$ give theoretical asymptotic gains of 11 and 20 for Stolt and Lu, respectively. The slightly better numerical gains than expected can be explained by the fact that the MATLAB implementation is favorable to matrix operations, and the FFT is optimized. This may give an advantage to *f-k* methods. However, even with a low-level implementation, *f-k* methods are expected to outperform time-domain PWI according to the complexity analysis. The images of size 1000×1000 presented in Fig. 6 were computed in 2.05 s with the Lu method, 3.8 s with the Stolt migration, and

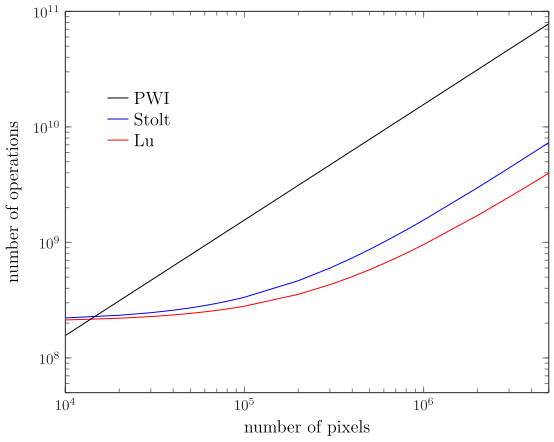

(a)

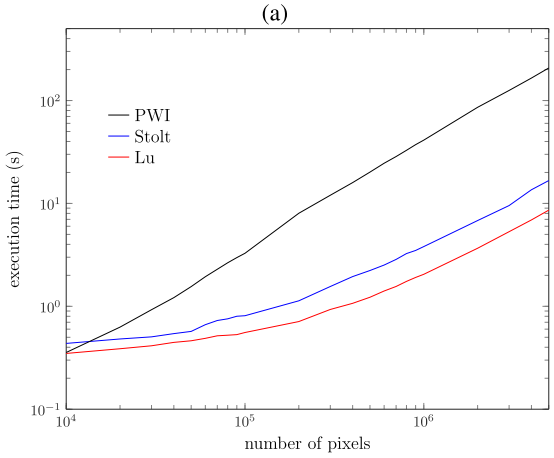

(b)

Fig. 9. (a) Algorithmic complexities as defined in (4), (33), and (36). (b) Computation times plotted according to the number of pixels.

41.4 s with PWI, yielding computational gains of 10.8 for Stolt and 20.1 for Lu.

V. Generalization of the *f-k* Methods to 3-D Imaging and Evaluation of Their Perfomances With Simulated and Experimental Data

In this section, the Lu and Stolt methods are generalized to 3-D imaging with matrix arrays. The theory is described hereafter for a contact array in order to be concise, and then the imaging algorithms are evaluated with immersion probes. In 3-D imaging, the extension of the *f-k* methods to immersion testing configurations is straightforward and follows the same principle of extrapolation of the wavefield as in 2-D imaging. As shown in Fig. 10, the array transmits a plane wave of polar angle θ and azimuth φ in the medium. The unit normal vector to the wavefront is

$$\mathbf{e}_{\theta,\varphi} = (\sin\theta\cos\varphi, \sin\theta\sin\varphi, \cos\theta). \tag{46}$$

The position vector of an element will be noted $\mathbf{u}_3 = (u, v, 0)$, and $\beta(\mathbf{r}, \mathbf{u}_3) = \arccos(z/\|\mathbf{r} - \mathbf{u}_3\|)$ is the polar angle under which $\mathbf{r}$ is seen from the receiver at $\mathbf{u}_3$. On the other hand, the Lu formalism extends to 3-D quite directly, one needs to

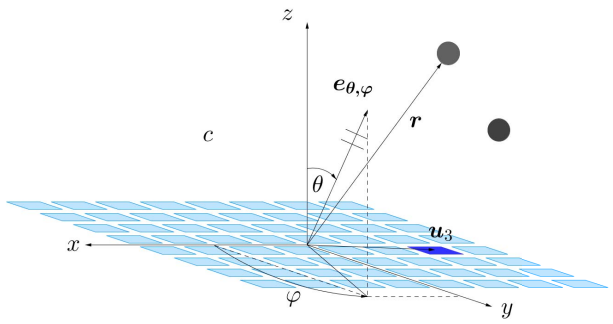

Fig. 10. Geometry and notations used in 3-D imaging with a matrix array. $\mathbf{e}_{\theta,\varphi}$ is the unit vector normal to the incident wavefront, where θ is the polar angle and φ the azymut.

generalize the ERM concept in 3-D for the Stolt method to be applicable.

A. Stolt Migration for 3-D Imaging

Following the same approach as in 2-D imaging, we derive here the ERM for the 3-D Stolt migration. The relationship between the sound velocities is still noted $\hat{c} = \alpha c$ and the spatial transformation is given by $\hat{\mathbf{r}} = \mathbf{r}\mathbf{T}$, with

$$\mathbf{T} = \begin{pmatrix} 1 & 0 & 0 \\ 0 & 1 & 0 \\ \gamma & \delta & \beta \end{pmatrix}. \tag{47}$$

Note that since the orientation of the x and y axis is arbitrary in the plane $\{z = 0\}$, α and β are independent of φ. The theoretical arrival time of a wave backscattered by a pointlike reflector at $\mathbf{r} = (x, y, z)$ and received at $\mathbf{u}_3 = (u, v, 0)$ is

$$\tau_{\mathbf{r}}(u, v) = \frac{1}{c}((\mathbf{r} - \mathbf{u}_3).\mathbf{e}_{\theta,\varphi} + \|\mathbf{r} - \mathbf{u}_3\|). \tag{48}$$

The corresponding arrival time in the virtual medium is

$$\hat{\tau}_{\mathbf{r}}(u, v) = \frac{1}{\hat{c}}\|\hat{\mathbf{r}} - \mathbf{u}_3\|. \tag{49}$$

As $\hat{\mathbf{r}} = \mathbf{r}\mathrm{T}$, the arrival time difference can be expressed as a function of the coordinates $\mathbf{r}$ in the physical medium, that is,

$$W_{\mathbf{r}}(u, v) = \frac{1}{c}[(\mathbf{r} - \mathbf{u}_3).\mathbf{e}_{\theta,\varphi} + \|\mathbf{r} - \mathbf{u}_3\|] - \frac{1}{\hat{c}}\|(\mathbf{r} - \mathbf{u}_3)\mathbf{T}\|. \tag{50}$$

Because the backscattered acoustic energy is concentrated around the apex of the diffraction hyperboloid, $\hat{c}$ and $\mathbf{T}$ must be such that the Taylor expansion of $W_{\mathbf{r}}(u, v)$ is zero at the highest order possible around $(u, v) = (x, y)$, regarding $W_{\mathbf{r}}(u, v)$ as a function of two variables. To do so, we first start by canceling the terms of orders 0 and 1, which writes

$$\begin{cases} W_{\mathbf{r}}(x, y) = 0 \\ \partial_u W_{\mathbf{r}}(x, y) = 0 \\ \partial_v W_{\mathbf{r}}(x, y) = 0. \end{cases} \tag{51}$$

Equation (51) imposes the following values of β, γ, and δ in function of α:

$$\begin{cases} \beta = \alpha(1 + \cos\theta)\sqrt{1 - \alpha^2\sin\theta^2} \\ \gamma = \alpha^2(1 + \cos\theta)\sin\theta\cos\varphi \\ \delta = \alpha^2(1 + \cos\theta)\sin\theta\sin\varphi. \end{cases} \tag{52}$$

The second-order Taylor expansion of $W_{\mathbf{r}}(u,v)$ around $(u,v)=(x,y)$ now only features order 2 terms and can be written using the Hessian $d^2W_{\mathbf{r}}(x,y)$ as

$$W_{\mathbf{r}}(u,v) \sim \frac{1}{2}(u-x, v-y)d^2W_{\mathbf{r}}(x,y)(u-x, v-y)^t. \quad (53)$$

Since α does not depend on φ, we can now consider $\varphi = 0$, and the Hessian takes the diagonal form

$$\begin{bmatrix} \dfrac{\alpha^2(1+\cos\theta)-1}{cz(1+\cos\theta)\alpha^2} & 0 \\ 0 & \dfrac{\alpha^2(1+\cos\theta+\sin^2\theta)-1}{cz(1+\cos\theta)\alpha^2} \end{bmatrix} = \begin{bmatrix} \mu_1 & 0 \\ 0 & \mu_2 \end{bmatrix} \quad (54)$$

where $\mu_2 - \mu_1$ is independent of α. Then, minimizing $|W_{\mathbf{r}}(u,v)|$ is equivalent to minimizing $\max(|\mu_1|,|\mu_2|)$. To do so, α must be chosen so that $\mu_2 = -\mu_1$, giving

$$|W_{\mathbf{r}}(u,v)| \underset{\substack{u\to x\\ v\to y}}{\sim} \frac{\sin^2\theta}{4cz(1+\cos\theta)}\|(x-u, y-v)\|^2. \quad (55)$$

In the general case where $\varphi \neq 0$, the coefficients of the ERM solving (52) and (55) are thus

$$\begin{cases} \alpha = \dfrac{1}{\sqrt{1+\cos\theta+\frac{1}{2}\sin^2\theta}} \\ \beta = 2\dfrac{\sqrt{1+\cos\theta-\frac{1}{2}\sin^2\theta}}{3-\cos\theta} \\ \gamma = \dfrac{2\sin\theta\cos\varphi}{3-\cos\theta} \\ \delta = \dfrac{2\sin\theta\sin\varphi}{3-\cos\theta}. \end{cases} \quad (56)$$

It can be observed that α and β remain unchanged compared to the 2-D case when $\theta = 0$. Now that the virtual medium is fully defined with $\hat{c}$ and $\mathbf{T}$, the Stolt method can be performed similar to the 2-D case. The reflector distribution $\hat{G}$ in the virtual medium is given by

$$\hat{G}(k_x,k_y,k_z) = \frac{\hat{c}k_z}{\sqrt{k_x^2+k_y^2+k_z^2}}S(k_x,k_y\omega) \quad (57)$$

where ω satisfies the 3-D dispersion equation

$$\omega = \hat{c}\ \mathrm{sign}(k_z)\sqrt{k_x^2+k_y^2+k_z^2}. \quad (58)$$

Finally, to get back in the physical medium, one only has to calculate $\hat{g}(x+\gamma z, y+\delta z, z)$ from the inverse total Fourier transform of (57).

From the implementation point of view, the Stolt mapping requires a trilinear interpolation that involves 28 additions and multiplications. Still by the symmetry of the Fourier spectrum, the interpolation is applied to half of the signal spectrum. For time-domain PWI, the linear interpolation of the signals is unchanged as far as the number of operations is concerned. Therefore, assuming $N_x, N_y \gg N$, the ratio of the algorithmic complexities between the PWI algorithm and the Stolt method writes

$$\frac{\mathcal{C}_P}{\mathcal{C}_S} \approx \frac{4N}{28+\log_2(N_z)}. \quad (59)$$

For example, if the number of voxels in the z-direction satisfies $\log_2(N_z) \approx 10$, and $N = 256$, the above ratio is close to 27.

B. Lu Method for 3-D Imaging

In order to derive the imaging equation of Lu, the forward model in (6) is extended to 3-D. In this case, the 3-D free space Green's function of the Helmholtz equation is used for the propagation of spherical waves back to the array

$$S(u,v,\omega) = A(\omega)\iiint e^{-i\mathbf{k}_{\theta,\varphi}.\mathbf{r}}g(\mathbf{r})\frac{e^{-ik\|\mathbf{r}-\mathbf{u}_3\|}}{\|\mathbf{r}-\mathbf{u}_3\|}dxdydz. \quad (60)$$

Once again, the Weyl identity allows rewriting the Green function as a sum of plane waves, that is,

$$\frac{e^{-ik\|\mathbf{r}-\mathbf{u}_3\|}}{\|\mathbf{r}-\mathbf{u}_3\|} = \iint \frac{e^{i\mathbf{K}\cdot(\mathbf{u}_3-\mathbf{r})}}{\sqrt{k^2-k_u^2-k_v^2}}dk_u dk_v \quad (61)$$

with

$$\mathbf{K} = \left(k_u, k_v, \sqrt{k^2-k_u^2-k_v^2}\right). \quad (62)$$

Next, following the same play on Fourier transforms as in the 2-D case, one gets

$$G(k_x,k_y,k_z) = \frac{\sqrt{k^2-k_u^2-k_v^2}}{A(\omega)}S(k_u,k_v,\omega) \quad (63)$$

with

$$\begin{cases} k_u = k_x - k\sin\theta\cos\varphi \\ k_v = k_y - k\sin\theta\sin\varphi \\ k = \dfrac{k_x^2+k_y^2+k_z^2}{2k_x\cos\varphi\sin\theta+2k_y\sin\varphi\sin\theta+2k_z\cos\theta}. \end{cases} \quad (64)$$

As for the Stolt method in 3-D, assuming $N_xN_y \gg N$, the ratio between the algorithmic complexities of PWI and the Lu method writes

$$\frac{\mathcal{C}_P}{\mathcal{C}_L} \approx \frac{4N}{28+\frac{\log_2(N_xN_yN_z)}{Q}}. \quad (65)$$

For $Q \geq 20$ and $N = 256$, this ratio is close to 36.

C. Results in 3-D Imaging With Immersion Matrix Arrays

In this section, we present results in 3-D imaging with immersion matrix arrays. In the first application, a lattice of spherical inclusions in a steel block is imaged by post-processing signals simulated with the CIVA software. All inclusions are below the matrix array aperture where the Stolt method remains valid and can then be compared with time-domain PWI and the Lu method. In the second application, images are performed with experimental data and the goal is to image simultaneously several crack-type defects with different orientations in a Dural specimen. All the defects are outside of the matrix aperture, and this experiment demonstrates the ability of the Lu method to produce very large volumes with low computations times.

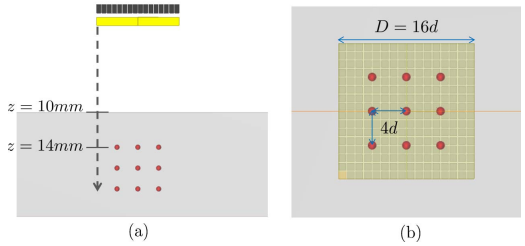

Fig. 11. Geometry of the lattice of inclusions. (a) Side view. (b) Bottom view.

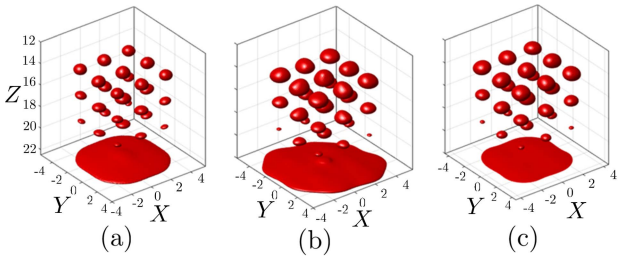

Fig. 12. Isosurface representations of the reconstructed volumes. (a) PWI. (b) Stolt. (c) Lu.

1) Imaging of Inclusions in a Volume of Base Area $D \times D$: To assess the performances of *f-k* domain methods in 3-D, we first studied a simulation case. As shown in Fig. 11, a ferritic steel block featuring a 3-D lattice of spherical inclusions is insonified by a 16×16 element matrix array immersed in water and positioned at 10 mm from the water/steel interface. The thickness of the specimen is 12 mm and longitudinal waves propagate with the phase velocity $c = 5.9$ mm $\cdot\, \mu s^{-1}$. The 2-D array operates around 5 MHz, and the pitch is identical in the x- and z-directions, i.e., $d = 0.6$ mm. The 27 inclusions are arranged in a 3-D lattice of period $4d$ in the three directions, and their diameter is d. The distance between the array and the horizontal plane of the 9 topmost inclusions is $z = 14$ mm, and $z = 18.8$ mm for the deepest ones. The RF signals were simulated in the CIVA software with 25 incident plane waves. They propagate inside the block according to the directions defined by the following polar and azimuthal angles (in degrees)

$$(\theta_k, \varphi_l) = \begin{cases} (0,0), & \text{if } k = 0 \\ (10k, 45l), & \text{otherwise} \end{cases} \tag{66}$$

with $k \in \{0, \ldots, 3\}$ and $l \in \{0, \ldots, 7\}$.

Time-domain PWI and both *f-k* migration methods were implemented in MATLAB, and the codes were run with the same computer as in the 2-D case. The 3-D images are displayed in Fig. 12 in the form of isosurfaces, each one corresponding to a percentage of the maximum amplitude in the whole volume. This percentage is 40% for the PWI image, and 30% for the Solt and Lu images. The base area of the each volume is $D \times D$ with $D = 16d$, and the number of voxels is $N_x \times N_y \times N_z = 100 \times 100 \times 490$. For the three images, the deepest inclusions at $z = 18.8$ mm appear smaller due to the amplitude decrease in depth, which can be corrected in practice with a time compensation gain. As in 2-D imaging, a greater amplitude damping with respect to the distance z is observed for the images computed in the Fourier domain. Similar to Section III, this can be interpreted by means of asymptotic expansions of the 3-D imaging equations, the calculation of which is detailed in Appendix B. For PWI, if we write $K(\mathbf{r}, u, v, \omega) = S(u, v, \omega) e^{ik(\mathbf{r}.\mathbf{e}_{\theta,\varphi} + \|\mathbf{u}_3 - \mathbf{r}\|)}$, the spectrum of the delayed signal received by an element of coordinates $\mathbf{u}_3 = (u, v, 0)$, the image amplitude at $\mathbf{r} = (x, y, z)$ for a single plane is given by

$$g_P(\mathbf{r}) = \int_{\mathbb{R}^3} K(\mathbf{r}, u, v, \omega) du dv d\omega. \tag{67}$$

Under the assumption that $z \gg \lambda$ for all frequencies in the transducer bandwidth, it is demonstrated in Appendix B that the imaging equations of Stolt and Lu can be rewritten in the following forms:

$$\frac{g_L(\mathbf{r})}{2\pi\sqrt{i}} \approx \int_{\mathbb{R}^3} \frac{k^2 \cos^2 \beta(\mathbf{r}, \mathbf{u}_3)}{\|\mathbf{r} - \mathbf{u}_3\|} K(\mathbf{r}, u, v, \omega) du dv d\omega \tag{68}$$

$$\frac{g_S(\mathbf{r})}{2\pi\sqrt{i}} \approx \int_{\mathbb{R}^3} \frac{\hat{k} \cos \beta(\hat{\mathbf{r}}, \mathbf{u}_3)}{\|\hat{\mathbf{r}} - \mathbf{u}_3\|} e^{i\omega W_{\mathbf{r}}(u,v)} K(\mathbf{r}, u, v, \omega) du dv d\omega \tag{69}$$

where $W_{\mathbf{r}}(u, v)$ is the arrival-time error defined in (50). In 3-D, the weighting functions of *f-k* methods feature $\|\mathbf{r} - \mathbf{u}_3\|$ and $\|\hat{\mathbf{r}} - \mathbf{u}_3\|$ at the denominator instead of $\|\mathbf{r} - \mathbf{u}_2\|^{1/2}$ and $\|\hat{\mathbf{r}} - \mathbf{u}_2\|^{1/2}$ in 2-D, which means that the image amplitude decreases more rapidly with respect to the distance from the array when the Stolt and Lu images are calculated in 3-D. In other terms, the amplitude differences between PWI and the *f-k* methods are always more significant in 3-D compared to those found in 2-D.

As for the spatial resolution, the difference between the PWI image and those calculated in the Fourier domain lies in the weighting coefficients k^2 and k, respectively, in (68) and (69), that filter the low-frequency content of the RF signals. The comparison of these coefficients with those highlighted in 2-D imaging [see (40) and (41)] shows that the *f-k* methods provide a better spatial resolution when they are implemented in 3-D, but this is generally counterbalanced by the smaller apertures of the matrix arrays compared to the linear probes. The second observation is that the Lu *f-k* migration is the best of the three methods in terms of spatial resolution since k^2 is a second-order high-pass filter (against a first-order filter for Stolt and no filter for PWI), which is confirmed by the xy cross sections in Fig. 13 displayed at different depths. For the Lu image, the spatial resolution is almost constant according to z, while it is more difficult to separate the echoes of the deepest inclusions with the Stolt method, and especially with time-domain PWI. In order to quantify the resolution improvement, Table II showcases the widths at -6 dB of the echoes located along the vertical central axis of the array. A_1, A_2, and A_3 denote the corresponding inclusions respectively located at $z_1 = 14$ mm (A_1), $z_2 = 16.4$ mm (A_2), and $z_3 = 18.8$ mm (A_3). For instance, for the deepest inclusion A_3, the Lu *f-k* migration improves the spatial resolution of nearly 17% compared to PWI, which is not negligible in 3-D imaging to compensate the loss of resolution due to the limited apertures of the matrix arrays.

TABLE II

WIDTHS AT −6 dB OF THE ECHOES OF THE CENTRAL INLCUSIONS AT $z_1 = 14$ mm (A_1), $z_2 = 16.4$ mm (A_2), AND $z_3 = 18.8$ mm (A_3)

Width at -6 dB					
	Width (mm)			Comparison with PWI	
Depth	PWI	Stolt	Lu	Stolt	Lu
4 mm	1.24	1.24	1.14	0%	-7.69%
6.4 mm	1.48	1.33	1.24	-9.78%	-16.13%
8.8 mm	1.71	1.48	1.43	-13.89%	-16.67%

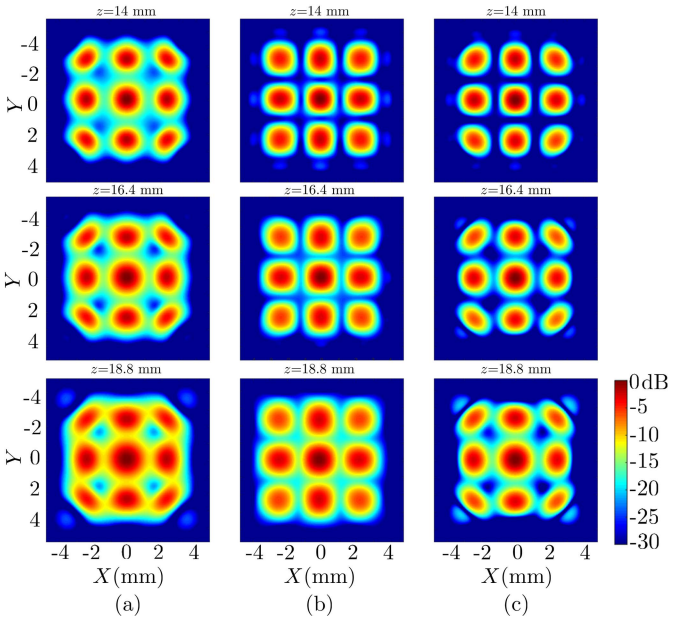

Fig. 13. xy cross sections of the 3-D images at $z_1 = 14$ mm, $z_2 = 16.4$ mm, and $z_3 = 18.8$ mm. (a) PWI. (b) Stolt. (c) Lu.

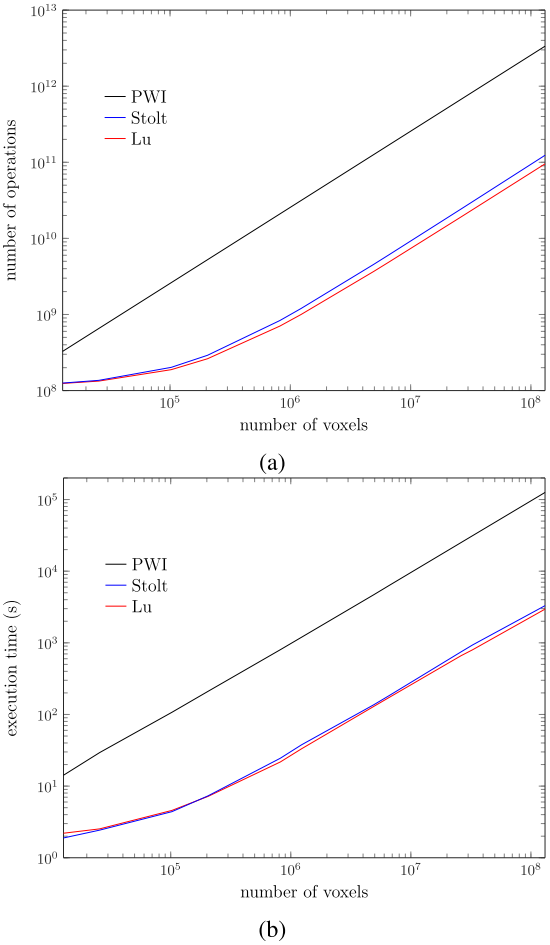

Fig. 14. (a) Algorithmic complexities and (b) computation times plotted according to the number of voxels.

Finally, regarding the computational performances in MATLAB, the reconstruction times and the algorithmic complexities are reported in Fig. 14. For a volume comprising $100 \times 100 \times 490$ voxels, the reconstruction times with 25 plane planes are 129.6 s for Lu, 136.8 s for Stolt, and 1h18 for PWI. Thus, in addition to providing images of better quality when noise is negligible, the *f-k* methods reduce the computation times by factors of 36 and 34. The gain for the Lu method coincides with the theoretical gain. For the Stolt migration, the reconstruction time seems to not be affected by the extra inverse FFT along the z-direction, which may explain why the computation times for both *f-k* methods are closer than expected.

The superiority of the Stolt method over PWI has to be tempered because it gives excellent results provided that all the reflectors are located under the matrix array. In the sequel, we are interested in the detection of crack-like defects that are beyond the aperture, requiring the formation of very wide 3-D images. As the Stolt method fails in such a situation, we will only compare the performances of time-domain PWI and the Lu method.

2) Imaging of Notches in a Volume of Base Area $5D \times 5D$: In this second NDT application involving a matrix array immersed in water, time-domain PWI and the Lu migration are applied to experimental data to form extended 3-D images with a base area $5D \times 5D$, where $D \times D$ is the matrix aperture. The sample is a Dural block ($c_L = 6.3$ mm $\cdot\, \mu$s^{-1}) featuring three identical backwall-breaking notches with a height of 5 mm and a length of 25 mm. As indicated in Fig. 15, the vertical notches have different skew orientations with respect to the z-axis; they are contained in three vertical planes describing an equilateral triangle. The experiment was carried out with a matrix array of 16×16 elements that operates around the central frequency $f_c = 5$ MHz (probe designed and distributed

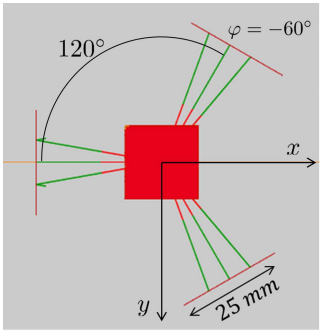

Fig. 15. Top view describing the experimental setup with an undersampled 16 × 16-element array and three breaking notches outside the array aperture.

by Imasonic, Voray-sur-L'Ognon, France). The array pitch is $d = 1.1$ mm in the x- and y-directions, and the active surface of the square elements is 1 mm^2. Signals were recorded with a multichannel MultiX++ system (M2M, Les Ulis, France). The water column height was set to 18 mm, and 27 steered planes waves with angles (in degrees)

$$\begin{cases} \theta \in \{35, 38, 45\} \\ \varphi \in \{-70, -60, -50, 50, 60, 70, 170, 180, 190\} \end{cases} \tag{70}$$

were transmitted to insonify the notches, as well as a horizontal plane wave to image the backwall. In order to avoid the presence of saturated signals related to the strong backwall echo, the preamplification gain was reduced by 20 dB for the horizontal plane wave compared to those transmitted at oblique incidence. Note that according to the spatial Nyquist criterion, d must satisfy the inequality

$$d \leq \frac{\lambda}{2} = 0.63 \text{ mm} \tag{71}$$

where $\lambda = c/f_c$. This inequality is not verified here since $d = 0.873\lambda$. This causes imaging artifacts around the notches due to secondary grating lobes that propagate toward the backwall when the defects are insonified with steered plane waves. In order to overcome the undersampling of the probe, zero traces were inserted in between real traces, which is equivalent to considering an array of 32×32 elements with a pitch of $d/2$ where only 256 elements are active in transmit and receive modes [34]. This procedure is not useful for time-domain PWI because inserting zero traces is equivalent to summing zero amplitudes. Due to the large size of arrays to be handled in the Lu method, both codes were run on an Intel Xeon 3.40-GHz CPU and 32 GB of RAM. The dimensions of the reconstructed zone are $87.5 \times 87.5 \times 10$ mm^3, and the number of voxels is $200 \times 200 \times 630 = 2.52 \times 10^7$. The compounded image of Lu was computed in 12 min and the reconstruction with PWI took 38 times longer, in agreement with the theoretical value 36 found in Section V-B.

In addition to reducing the computations times, the isosurface representations in Fig. 16 show that the Lu method gives an image quality equivalent to that provided by PWI. For both volumes, the same amplitude threshold corresponding to 40% of the maximum amplitude was used, and the presence of the strong backwall echo does not mask the defect echoes since the preamplification gain was lowered to record the signals associated with the horizontal plane wave. The 2-D representations in Fig. 17 are known in NDT as xy-echodynamic views and correspond to the projections of the maximum amplitude along the z-direction onto the xy plane. More clearly than the isosurface representations, they show that the 3-D imaging algorithms are able to characterize the orientations of several cracklike defects distributed in a large volume with an excellent contrast. It is to be noticed that the length of the echoes measured at -6 dB is roughly half the real length of the notches, i.e., 25 mm. This is due to the dimensions of the matrix array (17.6×17.6 mm^2) that are not large enough to fully image such long notches. For a better characterization of the defects, it would be necessary to perform reconstructions with a matrix of 32×32 elements,

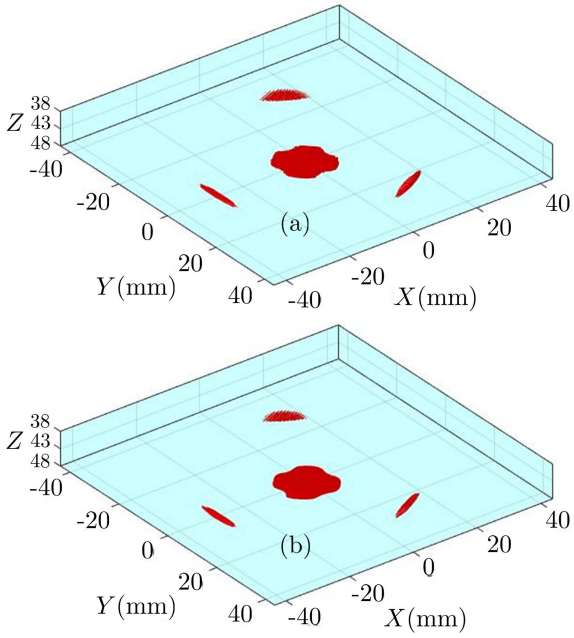

Fig. 16. Experimental 3-D images represented in the form of isosurfaces. (a) PWI and (b) Lu images.

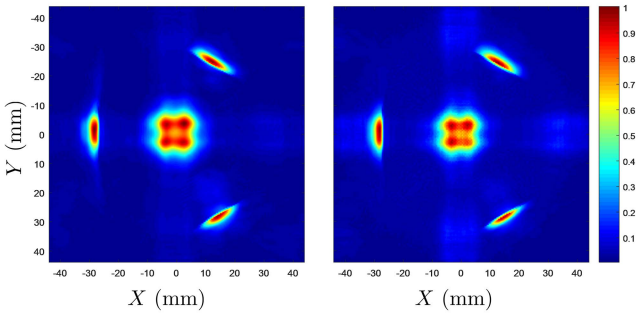

Fig. 17. Two-dimensional images in the xy plane corresponding to the maximum amplitude along the z-direction. (a) Lu and (b) PWI images.

which could be better managed with the method of Lu in terms of computation times.

VI. Conclusion

In this paper, we first recalled the imaging methods of Lu and Stolt for plane-wave emissions with contact arrays in 2-D. We gave a detailed rundown of the algorithms, leading to the derivation of the algorithmic complexities. In this simple case, it was shown that the Lu and Stolt methods were expected to operate $N/3$ and $2N/11$ times faster than PWI, respectively, where N is the number of elements of the array. Then, the 2-D algorithms were extended to deal with plane water/steel interfaces using similar wavefield extrapolation schemes, the computational cost of which being negligible compared to the remaining operations needed to form an image. This was confirmed by an analysis of the algorithm runtimes, which showed that the numerical gains were close, yet slightly higher, than the complexity gains. More specifically, the proposed MATLAB implementation of the Lu method operated up to 24 times faster than PWI with a 64-element array. A theoretical study of the image amplitudes then lead

us to predict the graphic performances of the algorithms. These previsions were confirmed by comparing images of side-drilled hole pairs in an area three times as wide as the array aperture. We showed that the Lu method improves the lateral resolution and that it is equivalent to applying a space–frequency filter in the PWI algorithm. Applying this filter to PWI could, thus, improve the image resolution, but it would be at the cost of computation efficiency, since signals would need to be Fourier transformed before being summed. More importantly, we exhibited a limit of the Stolt migration. Due to significant propagation time errors intrinsic to the definition of the ERM, the Stolt method is not fit to image defects beyond the array aperture. PWI and the methods of Stolt and Lu were then generalized to 3-D imaging with matrix arrays immersed in water. Carrying out a similar analysis as in the 2-D case, we proved that the Stolt and Lu methods were expected to be 27 and 36 times faster than PWI in 3-D with a matrix array of 16×16 elements. A first series of results obtained from simulated echoes aimed at comparing the performances of the imaging methods when pointlike defects are located under the matrix array aperture. It was shown in this configuration that the Stolt and Lu methods were asymptotically 34 and 36 times faster than PWI, respectively. Then, experiments were carried out with a specimen featuring several cracklike defects in a large volume, the base area of which is 25 times larger than the matrix array surface. The 3-D images calculated with PWI and the Lu method are almost identical (the Stolt method is invalid because defects must be detected at high angles), but the second one offers the advantage of reducing the computation times by a factor of 38, as predicted.

The computational study dwelled on the number of operations and algorithmic complexities. However, the amount of memory space required to operate the methods also has to be taken into account. It turns out that *f-k* migrations are less memory-efficient than PWI since they operate on large arrays of numbers for the interpolation and FFT steps. When running these algorithms on a system with insufficient RAM, the memory may get saturated, in which case the whole reconstruction significantly slows down.

The computation times stated in this paper in 3-D imaging are still far from real time. Parallelization seems to be a reasonable way to further accelerate image reconstruction. Delay and sum methods, such as PWI, would be trivially parallelizable, by assigning a processor to each element for instance. Even if such a simple parallelization would not suit a Fourier method implementation, the FFT is parallelizable on multiple graphics processing units [36], [37] and the interpolation step can be parallelized by segmenting the $k_x - k_y - k_z$ spectrum into subdomains. The parallelization of $f - k$ methods will be investigated in the near future.

Finally, what comes out of the comparison between Fourier domain algorithms and time-domain PWI is that *f-k* methods are especially performant under the array, in which case the lateral resolution is improved and the reconstruction times tremendously reduced. Future works will involve imaging with half-skip modes to improve the sizing of crack-like defects, such as in TFM or PWI [8], and additional experimental studies of the *f-k* methods in the presence of strong noise.

Appendix A
Derivation of the Asymptotic Image Amplitudes for 2-D *f-k* Methods

In the proof that follows, the three imaging equations from Section II are rewritten in the form of integrals over the receivers and frequencies. The aim is to emphasize the relationships between the image amplitudes for a single plane wave. Using (9), the image amplitude for the Lu method at a point $\mathbf{r} = (x, z)$ can be written as

$$g_L(\mathbf{r}) = \iiint \sqrt{k^2 - k_x^2}\, du\, dk_x\, d\omega \times S(u,\omega) e^{i\left(k\cos\theta + \sqrt{k^2-k_x^2}\right)z + ik_x(x-u) + ikx\sin\theta} \quad (72)$$

and the image obtained with time-domain PWI can be written in the frequency domain as well

$$g_P(\mathbf{r}) = \iint S(u,\omega) e^{ik\left(z\cos\theta + x\sin\theta + \sqrt{(x-u)^2+z^2}\right)} du\, d\omega. \quad (73)$$

To compare these two equations, we need to calculate

$$I(u,\omega) = \int \sqrt{k^2 - k_x^2} \times e^{i\left(k\cos\theta + \sqrt{k^2-k_x^2}\right)z + ik_x(x-u) + ikx\sin\theta} dk_x. \quad (74)$$

Integrals of the form

$$J_\alpha = \int f(s) e^{i\alpha h(s)} ds \quad (75)$$

where $f(s)$ and $h(s)$ are functions of a single variable s and $\alpha \to \infty$ can be expressed using the method of stationary phase through the asymptotic formula [35]

$$J_\alpha \sim \sqrt{\frac{2\pi}{\alpha |h''(s_0)|}} f(s_0) e^{i\alpha h(s_0) + i\mu\frac{\pi}{4}} \quad (76)$$

where s_0 is a stationary point of $h(s)$, i.e., satisfying $h'(s_0) = 0$, and $\mu = \text{sign}(h''(s_0))$. Here, we let $\alpha = kz$ because $z \gg \lambda$ for points sufficiently far away from the array located at $z = 0$. Moreover, with the notation $\Delta x = x - u$ and $R = (\Delta x^2 + z^2)^{1/2}$, (80) can be rearranged in the form

$$I(u,\omega) = \int e^{ikz\left[\left(\cos\theta + \sqrt{1-\left(\frac{k_x}{k}\right)^2}\right) + \frac{k_x\Delta x + kx\sin\theta}{kz}\right]} dk_x. \quad (77)$$

Comparing (77) with (75), we get $\alpha = kz$, $f(k_x) = (k^2 - k_x^2)^{1/2}$ and define

$$h(k_x) = \cos\theta + \sqrt{1 - \left(\frac{k_x}{k}\right)^2} + \frac{k_x\Delta x + kx\sin\theta}{kz}. \quad (78)$$

The stationary frequency k_{x_0} of h is

$$k_{x_0} = \frac{k\Delta x}{R}. \quad (79)$$

Provided $kz \gg 1$, (75) can be applied to $I(u,\omega)$, yielding

$$I(u,\omega) \approx \frac{\sqrt{2i\pi k}z^2}{R^{5/2}} e^{ik\left(x\sin\theta + z\cos\theta + \sqrt{(x-u)^2+z^2}\right)}. \quad (80)$$

Noting $K(\mathbf{r},u,\omega) = S(u,\omega)e^{ik(z\cos\theta+x\sin\theta+(x-u)^2+z^{2^{1/2}})}$, we obtain the following amplitudes for the PWI image and for that calculated with the Lu migration, respectively,

$$g_P(\mathbf{r}) = \iint K(\mathbf{r},u,\omega)dud\omega \tag{81}$$

and

$$g_L(\mathbf{r}) \approx \iint \frac{\sqrt{2i\pi}k^{3/2}z^2}{\|\mathbf{r}-\mathbf{u}_2\|^{5/2}}K(\mathbf{r},u,\omega)dud\omega. \tag{82}$$

Proceeding similarly with the Stolt method, i.e., starting from (18), the distribution of reflectors in an ER medium of celerity $\hat{c}$ can be written as

$$\hat{g}_S(\mathbf{r}) \sim \iint \frac{\sqrt{2i\pi\hat{k}}z}{\|\mathbf{r}-\mathbf{u}_2\|^{3/2}}\hat{S}(u,\omega)e^{i\hat{k}\|\mathbf{r}-\mathbf{u}_2\|}dud\omega \tag{83}$$

where $\hat{S}(u,\omega)$ is the wavefield at $z=0$ generated by the explosion. Using the fact that $\hat{S}(u,\omega) = S(u,\omega)e^{iku\sin\theta}$ and

$$g_S(\mathbf{r}) = \hat{g}_S(\hat{\mathbf{r}}) \tag{84}$$

we obtain

$$g_S(\mathbf{r}) \sim \iint \frac{\sqrt{2i\pi\hat{k}}\hat{z}}{\|\hat{\mathbf{r}}-\mathbf{u}_2\|^{3/2}}S(u,\omega)e^{i\hat{k}\|\hat{\mathbf{r}}-\mathbf{u}_2\|+iku\sin\theta}dud\omega. \tag{85}$$

Now, according to the theory in Section II-C2, α, β, and δ are such that

$$\frac{\|\hat{\mathbf{r}}-\mathbf{u}_2\|}{\hat{c}} = \frac{(x-u)\sin\theta+z\cos\theta+\|\mathbf{r}-\mathbf{u}_2\|}{c}+W_{\mathbf{r}}(u). \tag{86}$$

Finally, with the notations introduced earlier

$$g_S(\mathbf{r}) \sim \iint \frac{\sqrt{2i\pi\hat{k}}\hat{z}}{\|\hat{\mathbf{r}}-\mathbf{u}_2\|^{3/2}}e^{i\omega W_{\mathbf{r}}(u)}K(u,\omega)dud\omega. \tag{87}$$

Note that $W_{\mathbf{r}}(u)$ is only equal to 0 when $u=x$, therefore, arrival time errors in the ERM affect every pixel of the image, especially for pixels located away from the array aperture.

Appendix B
Derivation of the Asymptotic Image Amplitudes for 3-D *f-k* Methods

Using (69), the amplitude $g_L(\mathbf{r})$ of the Lu image at a point $\mathbf{r}$ is given by

$$g_L(\mathbf{r}) = \iiint I(u,v,\omega)S(u,v,\omega)dudvd\omega. \tag{88}$$

Proceeding as above in the 2-D case, we define

$$\begin{aligned} &I(u,v,\omega)\\ &= \iint \sqrt{k^2-k_x^2-k_y^2}e^{i\left(k\cos\theta+\sqrt{k^2-k_x^2-k_y^2}\right)z}\\ &\quad\times e^{i(k_x(x-u)+kx\sin\theta\cos\phi)+i(k_y(y-v)+ky\sin\theta\sin\phi)}dk_udk_v. \end{aligned} \tag{89}$$

Integrals of the form

$$J_\alpha = \int f(s,t)e^{i\alpha h(s,t)}dsdt \tag{90}$$

where $f(s,t)$ and $h(s,t)$ are function of 2 variables and $\alpha\to\infty$ can be expressed using the method of stationary phase through the asymptotic formula [38], that is,

$$J_\alpha \sim \frac{2\pi}{\alpha\sqrt{\det|H(s_0,t_0)|}}f(s_0,t_0)e^{i\alpha h(s_0,t_0)+i\mu\frac{\pi}{4}} \tag{91}$$

where (s_0,t_0) is a stationary point of $h(s,t)$, i.e., satisfying $\nabla h(s_0,t_0)=0$ and H is the Hessian matrix of h. We thus define $f(k_u,k_v) = (k^2-k_x^2-k_y^2)^{1/2}$ and

$$\begin{aligned} h(k_u,k_v) &= \cos\theta+\sqrt{1-\left(\frac{k_x}{k}\right)^2-\left(\frac{k_y}{k}\right)^2}\\ &\quad+\frac{k_x(x-u)+kx\sin\theta\cos\varphi}{kz}\\ &\quad+\frac{k_y(y-v)+ky\sin\theta\sin\varphi}{kz} \end{aligned} \tag{92}$$

and apply (91) to $I(u,v,\omega)$, yielding

$$g_L(\mathbf{r}) \approx \iiint \frac{2\sqrt{i}\pi k^2z^2}{\|\mathbf{r}-\mathbf{u}_3\|^3}K(\mathbf{r},u,v,\omega)dudvd\omega. \tag{93}$$

In a similar fashion, we derive

$$g_S(\mathbf{r}) \approx \iiint \frac{2\sqrt{i}\pi\hat{k}\hat{z}}{\|\hat{\mathbf{r}}-\mathbf{u}_3\|^2}e^{i\omega W_{\mathbf{r}}(u,v)}K(\mathbf{r},u,v,\omega)dudvd\omega. \tag{94}$$

Acknowledgment

The authors would like to thank G. Daniel and J. B. Boy from CEA List for their help in the experimental setup.

References

[1] M. Njiki, A. Elouardi, S. Bouaziz, O. Casula, and O. Roy, "Total focusing method for non destructive evaluation: Toward real-time imaging systems," in *Proc. IEEE 56th Int. Midwest Symp. Circuits Syst.*, Aug. 2013, pp. 1164–1167.

[2] M. Sutcliffe, M. Weston, B. Dutton, P. Charlton, and K. Donne, "Real-time full matrix capture for ultrasonic non-destructive testing with acceleration of post-processing through graphic hardware," *NDT&E Int.*, vol. 51, pp. 16–23, Oct. 2012.

[3] F. Reverdy, G. Benoist, and L. Le Ber, "Advantages and complementarity of phased-array technology and total focusing method," in *Proc. 19th World Conf. Non-Destructive Test.*, 2016, pp. 1–8.

[4] B. W. Drinkwater and P. D. Wilcox, "Ultrasonic arrays for non-destructive evaluation: A review," *NDT&E Int.*, vol. 39, no. 7, pp. 525–541, 2006.

[5] C. Holmes, B. W. Drinkwater, and P. D. Wilcox, "Post-processing of the full matrix of ultrasonic transmit–receive array data for non-destructive evaluation," *NDT&E Int.*, vol. 38, pp. 701–711, Dec. 2005.

[6] G. Montaldo, M. Tanter, J. Bercoff, N. Benech, and M. Fink, "Coherent plane-wave compounding for very high frame rate ultrasonography and transient elastography," *IEEE Trans. Ultrason., Ferroelectr., Freq. Control*, vol. 56, no. 3, pp. 489–506, Mar. 2009.

[7] L. Le Jeune, S. Robert, E. L. Villaverde, and C. Prada, "Multimodal plane wave imaging for non-destructive testing," in *Proc. ICU Int. Congr. Ultrason.*, 2015, pp. 570–573.

[8] L. Le Jeune, S. Robert, E. L. Villaverde, and C. Prada, "Plane wave imaging for ultrasonic non-destructive testing: Generalization to multi-modal imaging," *Ultrasonics*, vol. 64, pp. 128–138, Jan. 2016.

[9] J. Provost *et al.*, "3D ultrafast ultrasound imaging *in vivo*," *Phys. Med. Biol.*, vol. 59, no. 19, pp. L1–L13, 2014.

[10] J. Provost, C. Papadacci, C. Demene, J.-L. Gennisson, M. Tanter, and M. Pernot, "3-D ultrafast Doppler imaging applied to the noninvasive mapping of blood vessels *in vivo*," *IEEE Trans. Ultrason., Ferroelectr., Freq. Control*, vol. 62, no. 8, pp. 1467–1472, Aug. 2015.

[11] M. Yang *et al.*, "High volume rate, high resolution 3D plane wave imaging," in *Proc. IEEE Int. Ultrason. Symp.*, Sep. 2014, pp. 1253–1256.
[12] M. Karaman, I. O. Wygant, Ö. Oralkan, and B. T. Khuri-Yakub, "Minimally redundant 2-D array designs for 3-D medical ultrasound imaging," *IEEE Trans. Med. Imag.*, vol. 28, no. 7, pp. 1051–1061, Jul. 2009.
[13] R. H. Stolt, "Migration by Fourier transform," *Geophysics*, vol. 43, no. 1, pp. 23–48, 1978.
[14] A. J. Berkhout, "The seismic method in the search for oil and gas: Current techniques and future developments," *Proc. IEEE*, vol. 74, no. 8, pp. 1133–1159, Aug. 1986.
[15] M. H. Skjelvareid, T. Olofsson, Y. Birkelund, and Y. Larsen, "Synthetic aperture focusing of ultrasonic data from multilayered media using an omega-K algorithm," *IEEE Trans. Ultrason., Ferroelectr., Freq. Control*, vol. 58, no. 5, pp. 1037–1048, May 2011.
[16] D. Garcia, L. Le Tarnec, S. Muth, E. Montagnon, J. Porée, and G. Cloutier, "Stolt's f-k migration for plane wave ultrasound imaging," *IEEE Trans. Ultrason., Ferroelectr., Freq. Control*, vol. 60, no. 9, pp. 1853–1867, Sep. 2013.
[17] G. Franceschetti and G. Schirinzi, "A SAR processor based on two-dimensional FFT codes," *IEEE Trans. Aerosp. Electron. Syst.*, vol. 26, no. 2, pp. 356–366, Mar. 1990.
[18] R. Bamler, "A comparison of range-Doppler and wavenumber domain SAR focusing algorithms," *IEEE Trans. Geosci. Remote Sens.*, vol. 30, no. 4, pp. 706–713, Jul. 1992.
[19] T. Stepinski, "An implementation of synthetic aperture focusing technique in frequency domain," *IEEE Trans. Ultrason., Ferroelectr., Freq. Control*, vol. 54, no. 7, pp. 1399–1408, Jul. 2007.
[20] H. J. Callow, M. P. Hayes, and P. T. Gough, "Wavenumber domain reconstruction of SAR/SAS imagery using single transmitter and multiple-receiver geometry," *Electron. Lett.*, vol. 38, no. 7, pp. 336–338, 2002.
[21] W. C. Chew, *Waves and Fields in Inhomogeneous Media*. New York, NY, USA: IEEE Press, 1995.
[22] A. J. Hunter, B. W. Drinkwater, and P. D. Wilcox, "The wavenumber algorithm for full-matrix imaging using an ultrasonic array," *IEEE Trans. Ultrason., Ferroelectr., Freq. Control*, vol. 55, no. 11, pp. 2450–2462, Nov. 2008.
[23] E. Moghimirad *et al.*, "Synthetic aperture ultrasound Fourier beamformation using virtual sources," *IEEE Trans. Ultrason., Ferroelectr., Freq. Control*, vol. 63, no. 12, pp. 2018–2030, Dec. 2016.
[24] J.-Y. Lu, "2D and 3D high frame rate imaging with limited diffraction beams," *IEEE Trans. Ultrason., Ferroelectr., Freq. Control*, vol. 44, no. 4, pp. 839–856, Jul. 1997.
[25] J.-Y. Lu, "Experimental study of high frame rate imaging with limited diffraction beams," *IEEE Trans. Ultrason., Ferroelectr., Freq. Control*, vol. 45, no. 1, pp. 84–97, Jan. 1998.
[26] J. Cheng and J.-Y. Lu, "Extended high-frame rate imaging method with limited-diffraction beams," *IEEE Trans. Ultrason., Ferroelectr., Freq. Control*, vol. 53, no. 5, pp. 880–899, May 2006.
[27] K. Gu, G. Wang, and J. Li, "Migration based SAR imaging for ground penetrating radar systems," *IEE Proc.-Radar, Sonar Navigat.*, vol. 151, no. 5, pp. 317–325, Oct. 2004.
[28] A. Velichko and P. D. Wilcox, "An analytical comparison of ultrasonic array imaging algorithms," *The J. Acoust. Soc. Amer.*, vol. 127, no. 4, pp. 2377–2384, 2010.
[29] M. Darmon, N. Leymarie, S. Chatillon, and S. Mahaut, "Modelling of scattering of ultrasounds by flaws for NDT," in *Ultrasonic Wave Propagation in Non Homogeneous Media* (Springer Proceedings in Physics), vol. 128. 2013, pp. 61–71.
[30] M. Darmon and S. Chatillon, "Main features of a complete ultrasonic measurement model: Formal aspects of modeling of both transducers radiation and ultrasonic flaws responses," *Open J. Acoust.*, vol. 3, no. 3A, pp. 43–53, 2013.
[31] E. L. Villaverde, S. Robert, and C. Prada, "Ultrasonic imaging of defects in coarse-grained steels with the decomposition of the time reversal operator," *J. Acoust. Soc. Amer.*, vol. 140, no. 1, pp. 541–550, 2016.
[32] E. Iakovleva, S. Chatillon, P. Bredif, and S. Mahaut, "Multi-mode TFM imaging with artifacts filtering using CIVA UT forwards models," *AIP Conf. Proc.*, vol. 1581, no. 1, p. 72, 2014.
[33] K. Sy, P. Brédif, E. Iakovleva, O. Roy, and D. Lesselier, "Development of the specular echoes estimator to predict relevant modes for total focusing method imaging," *NDT&E Int.*, vol. 99, pp. 134–140, Oct. 2018.
[34] P. L. M. J. van Neer and A. F. W. Volker, "Imaging beyond aliasing," in *Proc. IEEE Int. Ultrason. Symp.*, Oct. 2015, pp. 1–4.
[35] N. Bleistein and R. A. Handelsman, *Asymptotic Expansions of Integrals*. New York, NY, USA: Holt, Rinehart and Winston, 1975.
[36] C. P. da Silva, L. F. Cupertino, D. Chevitarese, M. A. C. Pacheco, and C. Bentes, "Exploring data streaming to improve 3D FFT implementation on multiple GPUs," in *Proc. 22nd Int. Symposium Comput. Archit. High Perform. Comput. Workshops*, Oct. 2010, pp. 13–18.
[37] S. Keskin, E. Erdil, and T. Kocak, "An efficient parallel implementation of 3D-FFT on GPU," in *Proc. IEEE High Perform. Extreme Comput. Conf.*, Sep. 2017, pp. 1–4.
[38] L. Hörmander, *The Analysis of Linear Partial Differential Operators*, 2nd ed. Berlin, Germany: Springer-Verlag, 1980.

Lucas Merabet was born in Beauvais, France, in 1992. He received the master's degree in engineering from Ecole Centrale Paris, Paris, France, in 2015, the master's degree in mathematics from the University of Cambridge, Cambridge, U.K., in 2015, and the Ph.D. degree in physics from PSL Research University, Paris, France, in 2019.

In 2015, he joined CEA-LIST, Gif-sur-Yvette, France. His research dwells on ultrasound imaging techniques in the Fourier domain and their applications to real-time nondestructive testing.

Sébastien Robert was born in Fécamp, France, in 1975. He received the master's degree in physical acoustics and the Ph.D. degree from Le Havre University in 2001 and 2005, respectively, with a focus on wave propagation in periodic and random multiple scattering media.

He held a CNRS postdoctoral position with the Langevin Institute, Paris, France. He was a Research Engineer in ultrasound imaging with CEA-LIST, Gif-sur-Yvette, France. Since 2009, he has been a Researcher with CEA-LIST. His research topics include multiple scattering in solids, time reversal techniques, real-time array imaging, and adaptive methods applied to complex geometries and materials.

Claire Prada was born in Paris, France, in 1962. She received the master's degree in mathematics from the École Normale Supérieure, Paris, and University Pierre et Marie Curie, Paris, in 1987 and received the Ph.D. degree in physical acoustics from University Paris Diderot, Paris, in 1991.

In 1990, she joined the Laboratoire Ondes et Acoustique, CNRS, Paris, as a Research Scientist. She is currently a Research Director with the Institut Langevin, Paris. She studies acoustic and elastic wave propagation using multielements methods and laser ultrasonic techniques. She was involved in time reversal acoustics and the related DORT method with applications in shallow water acoustics and ultrasonic imaging, and elastic guided waves, especially on zero group velocity and backward Lamb modes, and their applications to nondestructive evaluation.